

Dynamical Mass Measurements: Molecular Gas Emission in HD121617's Debris Disk

by

Joshua Andres Grajales
Class of 2024

A thesis submitted to the
faculty of Wesleyan University
in partial fulfillment of the requirements for the
Degree of Bachelor of Arts
with Departmental Honors in Astronomy

“Whatever you do, always give 100%. Unless you’re donating blood.”

– BILL MURRAY

Acknowledgments

To Meredith: Thank you to my research advisor Meredith for introducing me to the field of Astronomy. I enrolled in your Introduction to Astrophysics course my freshman year, my first exposure to Astronomy in an academic setting. Despite the course being remote due to COVID, the content you presented and your calculated pedagogical methods motivated me to join your research group the following year. With your guidance, you helped me discover my passions for research and data science, for this I am eternally grateful. Thank you for always supporting me, whether I needed help with course scheduling, academic work, or just someone to talk to. Thank you for encouraging me even through my struggles. Through your role as a professor, advisor, and mentor, I have learned more than I could have ever imagined. I can only hope to make you proud through my future professional endeavors.

To Ed, Roy, Seth, and Sarah: Thank you for teaching me technical skills that are fundamental for conducting research. Ed, thank you for your support through major planning and the REU process.

To the Disk Detectives: Thank you for helping me ramp up my coding skills in preparation for research. Thank you Anna for testing my HR diagram plotting tool. Thank you Hannah for helping me understand the code distribution to this project. Special thanks to Owen for helping me trouble shoot bugs while

coding. Shout-out to Eric and Jamar, I spent my first summer at Wesleyan doing research with you two.

This thesis is the culmination of two years of research at Wesleyan. I will always remember the feeling I had when I attended my first disk group meeting; as a freshman I was deeply intimidated by my peers as they all seemed to be speaking another language amid the debris disk jargon. If I could show this thesis to freshman Josh I think I'd make him proud. Little did he know that astronomy would open so many doors for him and the opportunity to explore the world.

Contents

1	Introduction	1
1.1	What is a Debris Disk	1
1.2	Anomalies: Debris Disks With Gas Abundance	4
1.3	Relevance of Debris Disks in Astronomy Research	6
1.4	Brief Review of Stellar Astrophysics	7
1.4.1	Hertzsprung-Russell (HR) Diagram	7
1.4.2	Pre-Main Sequence Stars	10
1.4.3	Spectral Type	11
1.4.4	Stellar Mass Measurements using Keplerian Rotation of Debris Disks	13
1.5	HD121617	15
1.6	Radio Astronomy	18
1.6.1	Overview	18
1.6.2	Components of an Interferometer: Instruments to Data	18
1.6.3	Advantages of Interferometry	19
1.6.4	ALMA	20
1.6.5	Observations and the u-v Plane	21
1.6.6	Source Sky Brightness to Visibilities	24

2	Observations	26
3	Results	28
3.1	Spectral Line Imaging	28
4	Analysis	35
4.1	Preparation of ALMA Data Set	35
4.2	An Introduction to MCMC	36
4.2.1	Background and Vocabulary	37
4.2.2	Modeling HD121617’s Debris Disk	38
4.3	Disk Object, Radiative Transfer, and Synthetic Images	42
4.4	Best Fit Parameters	44
5	Discussion	47
5.1	Comparison of Best Fit Parameters with the Literature	47
5.1.1	Millimeter Observations (ALMA) of HD121617	47
5.1.2	Scattered Light Observations of HD121617	49
5.2	Plotting Stellar Evolutionary Tracks and Isochrones	51
5.2.1	HR Plotting Tool	53
5.2.2	A Brief History of Dynamical vs Photometric Mass Mea- surement Techniques	55
5.2.3	HD121617: Dynamical vs. Spectroscopic Mass Measurements	58
5.2.4	Explaining the Discrepancies	60
6	Conclusion	62
6.1	Summary and Future Work	62
6.2	Acknowledgments	63

Chapter 1

Introduction

Debris disks are disks of gas and dust that orbit around solar systems much like the Kuiper and asteroid belt in our solar system. Debris disks are useful to investigate the architectural and dynamical evolution of solar systems. Debris disks support studies of exoplanets, as debris disks are indicators of successful planet formation and mass measurement techniques of stars in other solar systems.

1.1 What is a Debris Disk

Protoplanetary (or planet-forming) disks are composed of dense gas and dust surrounding a newly formed star. Ultimately, the contents of these protoplanetary disks, combined with their turbulent motions, serve as reservoirs of material from which planets eventually form (Andrews 2020; Williams & Cieza 2011). Over time, protoplanetary disks evolve into transition disks; a stage that some systems pass through with large cavities in their innermost, regions. Eventually, transition disks dissipate through some combination of stellar and planetary mechanisms (involving accretion, photoevaporation, winds, and the agglomeration of large solid bodies) (Hughes et al. 2018). Though each of these circumstellar disk phases share a common lineage, each should be regarded as distinct class of object.

The focus of our study is debris disks. Debris disks, like protoplanetary and transition disks, are both an outcome and an integral component of the formation

of planetary systems. Differences between these structures are reflected in 3 key characteristics:

- debris disks, generally, have lower gas-to-dust ratios
- debris disks are optically thin at all wavelengths
- debris disks are dominated by destructive rather than agglomerative processes

Generally, debris disks have lower gas-to-dust ratio in comparison to its protoplanetary and transition disk predecessors; a result of continuous gas accretion onto the central star and planets in earlier phases (Hughes et al. 2018) as well as photoevaporative winds. It should be noted, however, that debris disks are not just leftover remnants of protoplanetary and transition disks, but are rather structures whose dust content is continuously sustained through collisional processes (Poppe et al. 2000).

Dust grains in debris disks are derived from collisions of larger solids up to the size of planetesimals (Wyatt 2008). The emerging second-generation dust is continuously removed from the system by interaction with stellar radiation and stellar winds (Smirnov-Pinchukov et al. 2022). Sometimes, these planetesimals are composed of not only rock but also ice which, when eroded, releases gas molecules into the surrounding environment (Kral et al. 2017; Klusmeyer et al. 2021; Zuckerman & Song 2012; Kral et al. 2019).

The composition and origin of the gas in debris disks is uncertain, but may be consistent with second-generation rather than primordial molecular abundances. Smirnov-Pinchukov et al. (2022); Matr  et al. (2018); Klusmeyer et al. (2021) study the origin of gas-rich debris disks by probing the gas component of these

disks for molecular emission. Smirnov-Pinchukov et al. (2022) proposes that the origin of the gas can be deduced via other C-, O-, N-, S-bearing poly-atomic molecules that could have been retained from primordial matter in an earlier epoch of the circumstellar disk. In the past, the abundance of CO gas was believed to result from a primordial H_2 shielding mechanism (Visser et al. 2009). However, Smirnov-Pinchukov et al. (2022) mentions that H_2 shielding is probably not the dominant shielding mechanism for CO in debris disks. Instead Kral et al. (2017) shows that it's more likely that CO shielding results from neutral carbon, or C (a product of CO photodissociation). Other papers (Hughes et al. 2017; Klusmeyer et al. 2021) investigate whether second generation gas could result from comet-like molecules. This theory focuses on the study of cometary ice noting that, in addition to having water, carbon monoxide and carbon dioxide contents, also display traces of CH_4 , C_2H_2 , H_2CO , and HCN.

In previous sections we noted that debris disks, in comparison to protoplanetary and transition disks, are collisionally maintained and are generally characterized by low gas abundance. The optical depth of debris disks is the most practical criterion that helps distinguish them from protoplanetary and transition disk phases. Optical depth refers to the extent to which an observer can see through a material, versus how much it absorbs incident light. Optically thick media are those mediums where light is readily absorbed; optically thin mediums refer to those that absorb light to lesser degrees. The dust in debris disks is optically thin across all wavelengths whereas the dust in protoplanetary disks is optically thick at optical and infrared wavelengths.

1.2 Anomalies: Debris Disks With Gas Abundance

Kóspál et al. (2013) argued that the gas abundance in debris disks resulted from a high rate of cometary sublimation. Later studies (Kral et al. 2017) developed a second-generation gas model that attributed gas abundance in debris disk systems to volatile-rich solid bodies that could be predicted from the fractional luminosity of a debris disk. This model, however, could not explain the abundance of gas in very massive debris disks (Kral et al. 2017). Kral et al. (2019) would show that C shielding of CO could extend CO’s lifetime such that it could help explain massive debris disk systems. To further understand C shielding, Rollins & Rawlings (2012) found that neutral carbon, one of the products of CO when it photodissociates, absorbs the same wavelength of light needed to photodissociate CO. Unfortunately, the shielding mechanism described in Kral et al. (2019) also applies to primordial protoplanetary disks which does not aid us in our understanding of the origin of massive, young, gas-bearing debris disks.

Recent studies reveal that gas in bright debris disks around young A-type stars presents itself as a rule rather than an exception (Moór et al. 2017). As it stands, the origin of the gas abundance in these systems are difficult to explain in the context of current gas production models (Kral et al. 2019, 2017). In particular, the gas found in these A-star debris disk systems are isotopologues of CO with mass ranging over 5 orders of magnitude (Smirnov-Pinchukov et al. 2022).

To characterize the lifetime of CO in debris disks we must consider how it interacts with its surrounding environment via photodissociation, planetesimal collision, and shielding. Photodissociation is when a photon breaks the bonds

between atoms in a molecule. The lifetime of gas molecules in debris disk is limited by photodissociation (the breakdown of molecules under photon bombardment). CO shielding is the process by which photodissociation is mitigated due to the presence of obstructing gas or dust. Estimates reveal that the unshielded CO has a lifetime of 120 Myr (Visser et al. 2009). Such a short lifetime makes it difficult to sustain large reservoirs of CO as the expectation would be that most, if not all of the gas, would have photodissociated before the debris disk phase.

Past studies show that the abundance of CO in these systems allow for CO to photodissociate into neutral atomic C gas. The extra shielding provided by this C gas would prolong the lifetime of CO allowing it to accumulate significantly. The outer layer of these debris disks is composed of photodissociated products, C gas, which shield the inner layer. Consequently, the shielding extends the lifetime of the gas in the inner layers.

The high abundance of CO in A-star debris disks systems could be attributed to their youth as they are in an early phase of debris disk evolution. It is expected that younger debris disks transitioned from the transition disk phase recently which allows us to assume a form of hybridity in these structures especially as it relates to their contents. This being the case, it is possible that residual C gas could serve as a shielding agent thereby allowing for the observed accumulation of CO in debris disks. Though this explanation aims to predict the effects of shielding on the abundance of CO gas, it is still insufficient to determine whether the gas in the inner most layers are primordial or second-generation.

1.3 Relevance of Debris Disks in Astronomy Research

Searching for debris disks in extra-solar systems is the equivalent of searching for Kuiper belt analogues. Our solar system's debris disk is composed of two components, the zodiacal light which is composed of material from disintegration of Jupiter-family comets, and the Edgeworth-Kuiper Belt which consists of material from collisions of planetesimals (bodies composed of rocks and dust) near Neptune's orbit. Searching for extra-solar debris disks often reveals multiple components reinforcing the idea that planets are common in debris systems (Wyatt et al. 2015). Given the coupling between debris disk structures and the presence of planets embedded within them, systems with Kuiper belt analogues are important because they provide a unique opportunity to study older phases of extra-solar system architecture in addition to the composition of materials of exoplanets.

Beyond this, the abundance of gas in gas-bearing debris disks provides an opportunity to learn about stellar physics. In particular, precise and accurate stellar mass measurements can be attained using the molecular emission and Keplerian rotation profiles of disks. From Kepler's third law we can express the orbital velocity of our system $v_{orbital}$ as a function of distance (from the observer) d to then derive the stellar mass M_* :

$$\sqrt{\frac{GM_{star}}{d}} = v_{orbital}$$

where G is the gravitational constant. It should be noted that we measure $v_{orbital} \times \sin(i)$ where i is the inclination of the disk. It should also be noted that though the gas in debris disks are affected by gas pressure, Rosenfeld et al.

(2013) showed that the pressure effects are relatively small for protoplanetary disks. As previously mentioned, because the gas-to-dust ratio is expected to be lower in debris disks we then expect gas pressure effects to be smaller in the lower-gas-mass environments of a debris disk. The distance can be derived using *Gaia* parallax measurements:

$$\theta_{parallax} = \frac{1}{d}$$

The orbital velocities can be derived using Doppler shifts of molecular gas lines which can be estimated by producing spectrum plots (i.e flux density vs. velocity) of observational data. The stellar mass estimates produced using this technique are called dynamical mass measurements and are crucial components for understanding stellar evolution but also the thermal, radiative, and chemical conditions where planets form (Pegues et al. 2021; Perrot et al. 2023; Czekala et al. 2015, 2016).

1.4 Brief Review of Stellar Astrophysics

The focus of this thesis is using gas emission from debris disks to measure the mass of the central star. To this end, we dedicate this section to the review of fundamental characteristics of stars and stellar evolution.

1.4.1 Hertzsprung-Russell (HR) Diagram

The HR diagram is one of the most important tools to study stellar evolution in the context of key stellar characteristics. It was developed in the 1900s by Ejnar Hertzsprung and Henry Norris Russell. Traditionally the HR diagram plots the

temperature of a star (on the x-axis) against their luminosity (on the y-axis).

As a star ages, its path on the HR diagram is determined by the star's initial mass. The initial mass dictates its internal structure and mechanisms of energy production. As the star ages, it undergoes changes in spectral type (and thus temperature) as well as energy production mechanisms (and thus luminosity and absolute magnitude).

The aging of stars induces change in the overall characteristics of the stars causing them to traverse various paths along the HR diagram. There exists 3 main regions (or evolutionary stages) of the HR diagram, 1.1:

1. Stars spend most of their lives on the main sequence (stars whose energy production mechanism relies on the fusion of hydrogen to make helium in their cores) which runs from upper left (hot and luminous stars) to the bottom right (cool and faint stars) of the diagram.

2. Red giant and supergiant stars occupy the region above the main sequence. These stars are characterized by their low surface temperatures and high luminosities, which according to the Stefan-Boltzmann law (a law that helps us relate blackbody radiation to stellar size) tells us they also have large radii. Stars in this region are also characterized by the burning of helium and other elements in their cores – an auxiliary energy production mechanism used by stars once hydrogen content in the core is depleted.

3. White dwarf stars are stars that have reached their final evolutionary stage. They are generally characterized by intermediate mass stars and are found in the bottom left of the HR diagram. They are very hot but have low luminosities due to their small size.

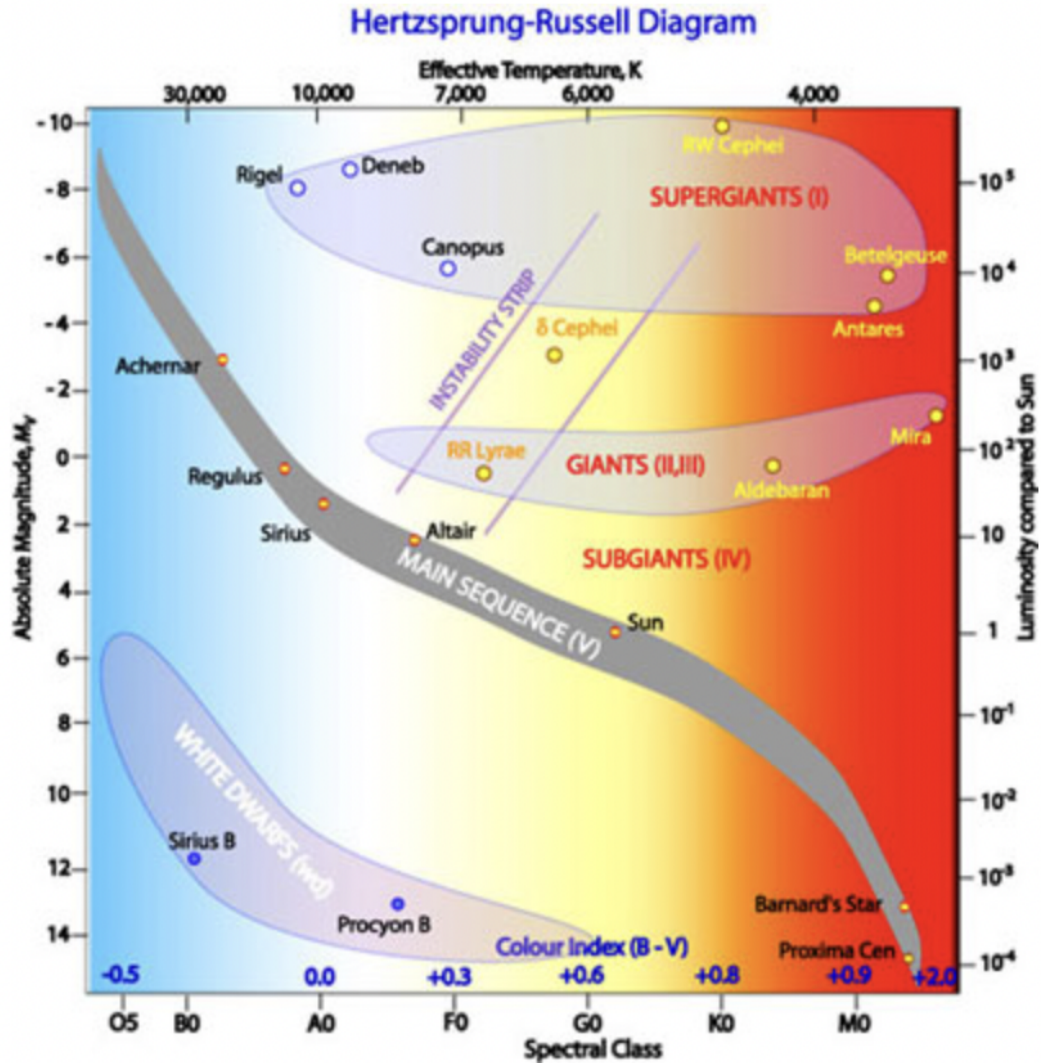


Figure 1.1: The Hertzsprung-Russell diagram describing the various stages of stellar evolution. The main sequence is shown in grey, which runs from the upper left (hot, luminous stars) to the bottom right (cool, faint stars) of the diagram. The giant branch and supergiant stars lie above the main sequence, and white dwarfs are found below it. The image was gathered from the Centre for Astrophysics and Super Computing at Swinburne University of Technology. Credit: R. Hollow, CSIRO.

1.4.2 Pre-Main Sequence Stars

Protostars, or clouds of gas and dust that form stars, grow from subsequent accretion of material. Once this cloud collapses turning into a star, the first stage of stellar evolution, the so-called pre-main-sequence or PMS begins. Physically, the gas collapses isotropically creating a star whose interior is heated from a release of gravitational potential energy (Kunitomo et al. 2017). The heat or energy released from the star is observed via its luminosity. At this point, the star is still in the PMS phase as it has not yet started hydrogen burning (i.e. nuclear fusion of hydrogen). The star then contracts, due to the forces of gravity induced by the material in its core. This period of contraction is the pre-main sequence stage. During this time the stars internal temperature rises until it begins burning hydrogen. Once the star begins burning hydrogen it has reached the second stage of stellar evolution, the main sequence.

The literature shows that PMS objects can either be a T Tauri (Johnstone et al. 2014) or Herbig Ae/Be (Wichittanakom et al. 2020) stars. Massive stars have no pre-main-sequence stage because they contract too quickly as protostars. In these situations, the hydrogen in their cores fuse immediately after the collapse of their molecular clouds and they are main-sequence objects.

The energy source of PMS objects is gravitational contraction, as opposed to hydrogen burning in main-sequence stars. In the Hertzsprung–Russell diagram, pre-main-sequence stars with more than $0.5 M_{\odot}$ first move vertically downward along Hayashi tracks, then leftward and horizontally along Henyey tracks, until they finally halt at the main sequence. Pre-main-sequence stars with less than $0.5 M_{\odot}$ contract vertically along the Hayashi track for their entire evolution.

PMS stars, have circumstellar disks, which are the sites of planet formation.

For this reason the disks that surround these PMS objects are called protoplanetary disks (Plavchan et al. 2020).

1.4.3 Spectral Type

In 1817 a German scientist, Joseph von Fraunhofer, attached a spectroscope to a telescope and pointed it at stars. He found that different stars had different absorption lines in their spectra. Later, in the early 1900s, a team of female astronomers at Harvard College Observatory performed further analysis of these spectra ultimately developing a detailed spectral classification system based on absorption lines.

The spectral classification system we use today assigns stars a letter based on the strength of Balmer series (a series of spectral line emissions of the Hydrogen atom) absorption lines. This new system ordered spectral classes **OBAFGKM** where O stars are the hottest and most massive and each successive star is cooler with M being the coolest and least massive. This classification scheme is only applicable to stars once they've reached the main sequence (i.e burn hydrogen in their cores). Over time, the spectral classification system has increased in granularity, dividing each letter into tenths by adding a number of 0-9 to the end. Figure 1.2 compares the relative size of stars as a function of their spectral type.

Through observations, astronomers have gathered that O stars are the least common and M are the most common on the main sequence. The table below summarizes the classification scheme describing the ranges of temperature corresponding to the spectral types of stars and their prevalence among stars on the main sequence.

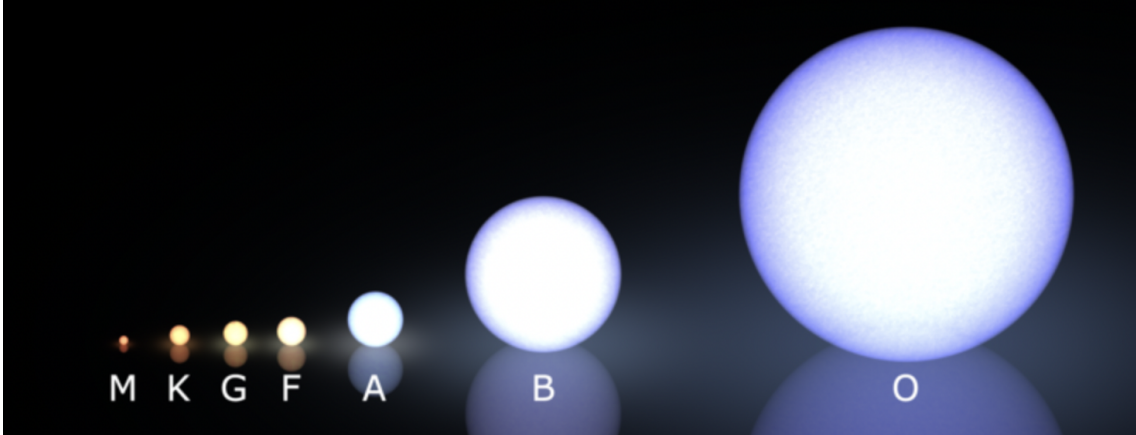


Figure 1.2: A cartoon image comparing the relative size of stars as a function of spectral types. Image credit Lucas VB as presented in Las Cumbres Observatory's Space Book.

Spectral Type	Color	Temperature Range	Prevalence Among Main Sequence Stars	Examples
O	Blue-Violet	$\geq 30,000\text{K}$	0.00003 %	Stars of Orion's Belt
B	Blue-White	10,000K - 30,000K	0.13%	Rigel
A	White	7,500K - 10,000K	0.6%	HD121617
F	Yellow-White	6,000K - 7,500K	3%	Polaris
G	Yellow	5,000K - 6,000K	7.6%	Sun
K	Orange	3,500K - 5,000K	12.1 %	Arcturus
M	Red-Orange	$\leq 3,500\text{K}$	76.5 %	Proxima Centauri

Figure 1.3: Describes the color and temperature range corresponding to stars of a given spectral type as well as their overall prevalence among main sequence stars. The data presented in this table was gathered from Las Cumbres Observatory's Space Book.

1.4.4 Stellar Mass Measurements using Keplerian Rotation of Debris Disks

Accurate characterization of star masses at young ages provides critical insight into their thermal and radiative environment, and consequently the chemical conditions where planets form (Pegues et al. 2021). Traditionally, astronomers utilize stellar evolutionary models to predict the masses of stars using observational estimates of their luminosities and effective temperatures. These stellar mass estimates then become crucial for understanding stellar evolution for both single star systems and entire star-forming regions. However, the ability to measure stellar masses for young, low-mass stars is one of theoretical difficulty because traditional heuristics simplify complex physics unique to this young stellar regime. Though these stellar evolutionary heuristics serve as a benchmark for estimating stellar masses, there are few alternative methods to compare the accuracy of these theoretical predictions. In the case of gas-bearing debris disk host stars, orbiting gas provides an important and rare opportunity to test the theoretical models from a new physical perspective.

The ability to estimate stellar masses using the Keplerian rotation pattern of gas in circumstellar disks is one recently acquired with the advent of the Atacama Large Millimeter/sub-millimeter Array (ALMA) and *Gaia*. Specifically, ALMA assists astronomer's in their observation of molecular line emission in these extra-solar systems by providing sufficient angular resolution to measure how the orbital velocity of gas varies with distance from the central star and high enough sensitivity to detect the faint emission of gas in these disks. *Gaia* offers precise distance measurements to these sources. Combined, these two instruments offer the astronomical community the ability to perform observations inaccessible to previous

generations of scientists. Previous generations of astronomers relied on detailed radiative transfer modeling of the Keplerian motion in spatially and spectrally resolved disks to estimate the mass of the host star (Dutrey et al. 1998). However the precision of these measurements were limited by large uncertainties (often greater than 10 percent) in the distances to the host star. This would result in imprecise measurements making it difficult to constrain the validity of stellar evolutionary models. It was not until *Gaia* that the uncertainties in distance measurements were significantly reduced.

Precise measurement of the fundamental parameters of stellar systems, including mass and radius, depends critically on how well the stellar distance is known (Al-Wardat et al. 2021). The *Hipparcos* satellite was the first space mission to be devoted to astrometry, or the measure of the positions, motions, and magnitude of celestial objects. It was not until 2013 that the European Space Agency (ESA) launched the *Gaia* mission which would obtain precise astrometry and photometry for approximately 1.7 billion stars, a 10,000 fold increase on *Hipparcos*. Past studies investigated the increased precision offered by the transition from *Hipparcos* to *Gaia* based parallax measurements. Overall the studies confirmed that dynamical masses, along with other physical parameters derived from parallax measurements, improved as a result of *Gaia* (Al-Wardat et al. 2021).

In the context of Kepler’s 3rd law, where here m is the mass of the gas:

$$T^2 = \frac{4\pi^2}{G(M_* + m)}a^3$$

the orbital period, T , can be derived using the radial velocity of the gas. The semi-major axis a , however is highly dependent on the distance. In this way, the precision of the stellar mass measurement is fundamentally limited by the

precision of the distance measurement.

Dynamical mass measurement techniques have various applications for the study of extra-solar systems. For example, MacGregor et al. (2017) uses dynamical mass measurement techniques to better understand the fundamental properties and underlying physical architecture of the GWOri system. Meanwhile, Ricci et al. (2017) uses dynamical mass measurement techniques to investigate the environments of a brown dwarf planetary mass system at unprecedented depth in terms of dust mass. Our study uses dynamical mass estimates to test stellar evolutionary models and thereby contribute towards the understanding of stellar physics and stellar evolution. We produce dynamical mass measurements and compare them to stellar evolutionary models in a sample of stars spanning tens to hundreds Myr in age. This is an unexplored regime of stars as previous studies were dedicated to comparing these techniques in M-dwarf, pre-MS, and binary systems. In the previously mentioned studies, the dynamical masses were in agreement with stellar evolutionary models. However Czekala et al. (2015) (pre-MS binary system) and Pegues et al. (2021) (M-dwarfs) find disagreement between their dynamical mass measurements and stellar evolutionary models. As such, discrepancies remain between the models and the direct measurements of stellar mass. The study of stellar masses is important because stellar mass estimates can shed insight on the disk-mass to stellar mass relation, how the two evolve with time, and the implication that this has on the planet formation process.

1.5 HD121617

In order to compare the dynamical and spectroscopic mass measurements of gas-bearing debris disk host stars, we perform a close study of HD121617. The

goal is to study all gas-bearing debris disk host stars in the literature. Currently, Meredith Hughes’ Disk Detective research group ¹ is developing studies of other gas-bearing debris disk host stars, producing dynamical masses of these systems and comparing them to stellar evolutionary models. By studying the complete sample of gas-bearing debris disk host stars, we hope to test stellar evolutionary models in an unexplored regime of stellar characteristics.

The earliest mentions of HD121617 was in 1978 where Nancy Houk studies a catalog of stars of the Pleiades Cluster. Here she reports a spectral type of A1V for HD121617 (Eggen 1983; Houk 1978). In 1992, Slawson et al. (1992) derives an absolute magnitude of 7.28 for HD121617 making it 9.5 times fainter than the sun. In 1998, HD121617 was first mentioned as a main sequence star with a debris disk (Mannings & Barlow 1998). Later studies, report a dust mass of $< 6 \times 10^{-6} M_{\odot}$ (Sylvester et al. 2001), while Krivov & Wyatt (2021) reports a dust mass of $2.8 \times 10^{-1} M_{\oplus}$ and a total disk mass of $4.3 \times 10^3 M_{\oplus}$. Discrepancy between these measurements likely results from their methods: Sylvester et al. (2001) uses millimeter observations and radiative transfer models to derive upper estimates on the dust mass whereas Krivov & Wyatt (2021) takes a dynamical approach using collisional cascade models to estimate the mass of disk. Smirnov-Pinchukov et al. (2022) reports an age of 16 and Pecaute & Mamajek (2016) reports an age of 16 ± 2 Myr. We note that Smirnov-Pinchukov et al. (2022) makes the simplification of quoting the age of the group HD121617 belongs to, UCL, while Pecaute & Mamajek (2016) derives the age based on the star formation history of their sample. Luminosity estimates cite $17 L_{\odot}$ (Moór et al. 2017), $14 L_{\odot}$ (Kral et al. 2019), and $17.3 L_{\odot}$ (Matrà et al. 2018). Though Moór et al. (2017) and Matrà et al. (2018) appear in close agreement, the discrepancy with Kral et al. (2019)’s

¹<http://amhughes.wescreates.wesleyan.edu/disk-detectives.html>

measurement is attributed to the their methods: Kral et al. (2019) measures luminosity using the optically thin CO isotopic lines whereas others derive the luminosity from global qualities of HD121617’s moving group. The literature reports a star mass of $1.9 M_{\odot}$ (Matrà et al. 2018) and $1.90^{+0.06}_{-0.05} M_{\odot}$ (Pearce et al. 2022). We note that Matrà et al. (2018)’s star mass was derived using MCMC and by assuming HD121617 had reached the main sequence. Pearce et al. (2022) also derives using MCMC sampling methods but also models the dynamics of the disk in the context of stirring and sculpting caused by moderate-mass planets on wide orbits.

The most recent estimations of the stellar parameters are reported in different studies, for example Rebollido et al. (2018) estimated the effective temperature 9285 K using the spectral synthesis programs ATLAS and SYNTHE. In Cotten & Song (2016), the effective temperature is estimated is 8710K and a stellar radius of $1.63 R_{\odot}$. Cotten & Song (2016) derives these values via SED fitting of using NEXTGEN and Kurucz model (Hauschildt et al. 1999). Here Cotten & Song (2016) acknowledges that the two models produce systematic differences of about 120K in the best fit stellar temperatures which helps explain the discrepancy with other T_{eff} estimates in the literature.

Spectral line data shows that HD121617’s debris disk has a CO gas mass of $1.8 \times 10^{-2} M_{\oplus}$ (Moór et al. 2017), while Kral et al. (2019) estimates a CO gas mass of $3 \times 10^{-3} M_{\oplus}$ placing it among the highest CO bearing debris disks. Specifically, Moór et al. (2017) finds that HD121617 has an optically thick CO ¹² with a $\tau \geq 30$, while CO ¹³ and C ¹⁸O is optically thin with $\tau \leq 5.7$. Moór et al. (2017) also cites a ¹² CO flux density of 1.27 ± 0.13 Jy km s⁻¹. Disk radius estimates report 83 au and a disk width of 60 au (Kral et al. 2019). Krivov & Wyatt (2021) reports a disk radius of 82.5 au and a disk width of 54.8 au.

1.6 Radio Astronomy

The data collected for this study is from the Atacama Large Millimeter Array (ALMA), an interferometer.

1.6.1 Overview

Visible-light astronomy reveals information about objects in optical light, or what we see with our eyes. However, visible light does not give us a complete understanding of celestial objects. To get a more holistic understanding of celestial objects astronomers study them in as many wavelengths as possible.

In comparison to optical waves, radio waves have a longer wavelength and a lower frequency. Radio wavelengths, spanning 30 kHz to 900 GHz, are imperceptible to the human eye. Each object in the cosmos gives off unique patterns of radio emissions that allow astronomers to study distant objects in ways optical astronomers cannot. Radio astronomers study emissions from molecular line emission, high energy blasts from the centers of galaxies, and pulsating stars, to name a few.

1.6.2 Components of an Interferometer: Instruments to Data

In its simplest form, a radio telescope has three components,

- **Antennas:** collects the incoming radio waves. Antennas are dishes that reflect the radio waves to a receiver in the same way optical telescopes reflect optical light using mirrors to a focus. In radio astronomy however, antennas

can also be other shapes. A Yagi antenna, similar to that used for TV reception.

- **Receiver and Amplifiers:** boost the weak radio signals to a measurable level. The relationship between energy and wavelength,

$$E = \frac{hc}{\lambda}$$

makes it clear that radio waves are low energy, especially in comparison to shorter, optical waves. Thus to increase sensitivity and boost signal, amplifiers were developed. In practice, these receivers are cooled to low temperatures to minimize interference generated by the movement of atoms in the surrounding environment.

- **Recorder:** keeps a record of the signal. In the past radio astronomers used a chart recorder that drew a graph on paper and ink. Today, most radio astronomers digitize the data collected by their instruments and perform their data analysis using supercomputers.

In order to produce images of radio sources, radio telescopes convert radio signals to data that can be used to make images. In the context of interferometers, data from the array of telescopes are brought together and processed in a computer.

1.6.3 Advantages of Interferometry

Radio waves, in comparison to optical waves, are less affected by absorption due to gas and dust in the interstellar medium. This allows us to detect sources obscured by gas and dust in optical observations.

Interferometers also offer higher angular resolution than is possible with optical telescopes. Interferometers have an effective angular proportional to the wavelength λ of the source and inversely proportional to the baseline D , or largest distance between telescopes in the array:

$$\theta_f = \frac{\lambda}{D}$$

. As a result, longer baseline configurations lead to higher angular resolution. The angular resolution of an interferometer is called the synthesized beam. The term synthesized beam is often paired with the term primary beam, which refers to an interferometers field of view. The primary beam is calculated by dividing the wavelength of observation by the diameter of the antennas in the array d :

$$\theta_b = \frac{\lambda}{d}$$

1.6.4 ALMA

We chose to study HD121617 using ALMA data because light at radio wavelengths provides the unique opportunity to study the chemical and physical conditions of this system. Additionally, observations in other wavelength ranges, such as optical, are less feasible because the light of HD121617 is not as bright in this range and suffers more from attenuation due to gas and dust in interstellar space.

Due to the fact that ALMA is the most sensitive millimeter instrument available, it is a great tool for supporting the study of debris disks. ALMA is capable of measuring both dust continuum and spectral line emission, giving us insight into the major components of circumstellar disks. ALMA is also 10x more sensitive and 10x higher resolution than previous telescopes that operated in this

wavelength range.

The ALMA site is in northern Chile and sits in a 5000-m high plateau. The dryness of this region in addition to its flat topography are good for millimeter interferometry as its high altitude mitigates the effects of water absorption in their observations and the flatness of the plane allows for the wide extension of its antennas allowing for larger baselines 1.4.

ALMA is composed of 66 antennas operating at wavelengths of 0.32 to 3.6mm. These antennas can be arranged in different configurations allowing for a baseline spanning 150m to 16km. For comparison, these baseline ranges give ALMA an angular resolution up to ten times sharper than the Hubble Space Telescope. The combined effects of ALMA's geographical location and engineering gives it unprecedented sensitivity and resolution.

1.6.5 Observations and the u-v Plane

A u-v plane is a geometric plane defined for the analysis of interferometric observations, for which the axes are conventionally termed u and v. The u-v plane is tangent to the celestial sphere at the position of the astronomical object under observation, with v chosen to be northward. The axes in the u-v plane are scaled using the wavelength of observations λ :

$$u = \frac{D}{\lambda} \cos \delta_B \sin(HA)$$

$$v = \frac{D}{\lambda} [\sin \delta_B \cos \delta_s - \cos \delta_B \sin \delta_s \cos(HA)]$$

where D is the baseline length, HA is the hour angle of the source, δ_B is the declination of the baseline, and δ_s is the declination of the source. The



Figure 1.4: Aerial view of the Chajnantor Plateau in northern Chile. The image shows the array of ALMA antennas. Image credit: Clem & Adri Bacri-Normier.

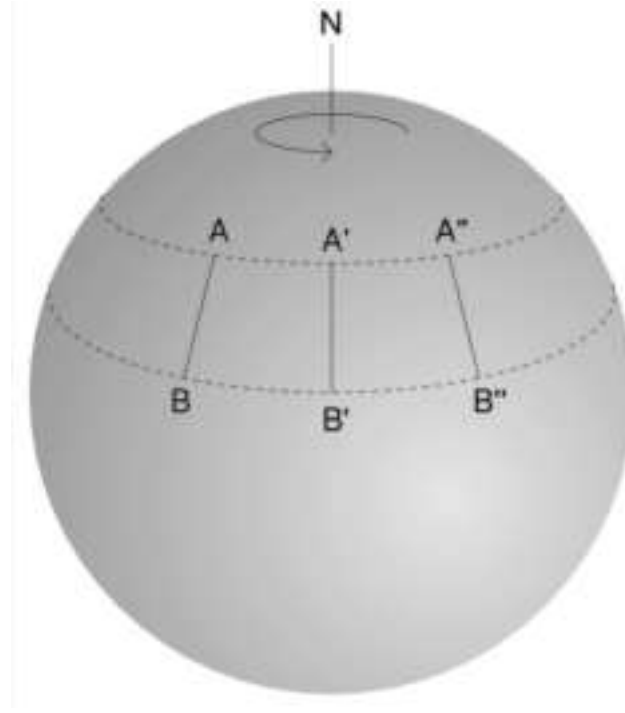


Figure 1.5: Using the Earth rotation the baseline length between telescopes A and B changes with angle as viewed from the source.

purpose of the u - v plane is to represent the Fourier transform of the signal from a portion of the sky. The result of this Fourier transform, which is the output of the interferometer correlator (a device that combines the signals from antennas in the array) are called visibilities. This result is formally named the Van Cittert-Zernike theorem.

Given the dependence of u and v on the δ_S and D , it is possible to sample points in the u - v plane by allowing the rotation of the Earth to increase the number of baseline orientations, a process called Earth rotation aperture synthesis 1.5. By using Earth rotation aperture synthesis, measurements can be taken at different times thereby increasing the number of data points in the u - v plane.

1.6.6 Source Sky Brightness to Visibilities

The response of ALMA to the brightness distribution of a source in the sky is a collection of measurements called complex visibilities. To define a visibility, we first define the response of a two-element interferometer. Once light from the source arrives to each of the antennas, a correlator combines the signals received. In order to understand how these signals are turned into visibilities we introduce some definitions; these are standard conventions as presented in the *Synthesis Imaging in Radio Astronomy* textbook ²:

- **Source Brightness** in direction s at frequency ν , $I_\nu(s)$, is measured in $\text{erg s}^{-1} \text{ cm}^{-2} \text{ Hz}^{-1} \text{ Sr}^{-1}$.
- $A(s)$ effective collecting area in direction s
- **Radiation Power** $I_\nu(s)A(s)\Delta\nu d\Omega$
- **b** baseline of two element interferometer, or the separation between the two antennas

If we assume that the source brightness extends over a small area in the sky we can rewrite $s = s_0 + \sigma$, where s_0 represents the phase center of the field of view. If we also assume that the source is far from the interferometer, to the point where the incoming waves of light are parallel to the plane of the antenna dishes, it can be shown that the response to a two-element interferometer to a source in the sky is:

$$V(b) = \int_{\Omega_s} A(\sigma) I_\nu(\sigma) e^{-2\pi i \nu b \sigma / c} d\Omega$$

²<https://leo.phys.unm.edu/~gbtaylor/astr423/s98book.pdf>

where Ω_s is the angular size of the source. However, in order to express the visibilities $V(b)$ in a practical form it is useful to write it in terms of baseline vectors (u, v) where u points east and v points north. Following the derivation in *Synthesis Imaging in Radio Astronomy*:

$$V(u, v) = \int_{-\infty}^{\infty} \int_{-\infty}^{\infty} A(l, m) I_{\nu}(l, m) e^{-2\pi i(ul+vm)} dldm$$

As we will see in Chapters 3 and 4, we create synthetic visibilities in order to model the data. In order to compare a model prediction to some observed visibilities $V_{obs}(u_k, v_k)$ (Tazzari et al. 2018) computes:

$$V_{mod}(u, v) = \int_{-\infty}^{\infty} \int_{-\infty}^{\infty} A(l, m) I_{\nu mod}(l, m) e^{-2\pi i(ul+vm)} dldm$$

and then samples V_{mod} at the same uv -points where the observations were taken.

Finally, we compare the model visibilities to the observed visibilities from the ALMA data. The quality of fit for each step is measured using a chi-square (χ^2) metric and is computed in the following way (Tazzari et al. 2018):

$$\chi^2 = \sum_{k=1}^M \chi_k^2 = \sum_{k=1}^M |(V_{obs}(u_k, v_k) - V_{mod}(u_k, v_k))|^2 w_k$$

where w_k is the weight associated with the k -th visibility.

Chapter 2

Observations

We used archival ALMA data to study HD121617. Our target was observed in the frequency range of 211 - 275 GHz (project 2015.1.01243.S, PI: M. Cure). Other studies have already been performed using this data as presented in Moór et al. (2017).

HD121617 was observed using ALMA on 2016 May 23. A total of 35 antennas were used during this observation with baseline lengths spanning 16.7-640 meters. Four spectral windows collected data associated with HD121617. Two of these windows were dedicated to continuum measurements providing MHz of bandwidth. These continuum spectral windows were centered at 217 MHz and 233.5 MHz. The remaining two spectral windows were tuned to cover the frequencies associated with the $J=2-1$ transitions of ^{12}CO (230.5380GHz), ^{13}CO (220.3987GHz), and C^{18}O (219.5603GHz) molecules. We chose to only model ^{12}CO (2-1) line because it has the highest signal to noise ratio and we are primarily interested in the dynamical mass of our system rather than the overall disk mass and structure. The spectral window containing data on ^{12}CO (2-1) was centered at 230.729 GHz with a bandwidth of 468.750 MHz, while the isotopologues lines were measured together in a window centered at 219.479 MHz with a bandwidth of 1875 MHz. The spectral resolutions in the two windows were 122.070 kHz and 488.281 respectively. Calibration and imaging was completed using the

standard ALMA data processing tool Common Astronomy Software Applications, CASA (McMullin et al. 2007). In preparation for the imaging, we used `cvel` to convert velocities into LSRK and `uvcontsub` to subtract continuum emission. To image our system we used the CASA `tclean` task using briggs weighting and a robust parameter of 2. The beam position angle, major axis, and minor axis are -5.99° , $1.83'' \times 1.67''$ respectively. Our measured RMS noise is -1.99×10^{-2} Jy beam $^{-1}$.

Chapter 3

Results

In this section, we present the images and basic properties of the disk based on the observations. Detailed modeling and corresponding results will be discussed in chapters 4 and 5.

3.1 Spectral Line Imaging

Line Data - We began by CO(2-1), 230.5380GHz, using the **split** command. In the split command, we used a timebin of 25 seconds and a channel width of 2. Our time averaging was warranted because our data had higher-than-necessary spectral resolution. Once we identified the channels with emission, we used the **tclean** task to produce spectral cubes of the data. Spectral cubes are intensity images of the gas emission across frequency (i.e channel or velocity). The channel maps, or spectral cube, is presented in 3.1 along with the residuals of our modelling. We also used briggs weighting, a robust parameter of 2, and centered our channels around the CO(2-1) frequency.

We detected ^{12}CO emission in the disk. The peak flux density in each 0.3175 km s^{-1} -wide channel is 6 mJy beam^{-1} . We measured the flux density by locating the channel with most intense emission in the tcleaned channel maps.

We also produced moment 0 3.2 and moment 1 3.3 maps of the emission using the **immoments** task. Moment 0 maps are velocity integrated images of the

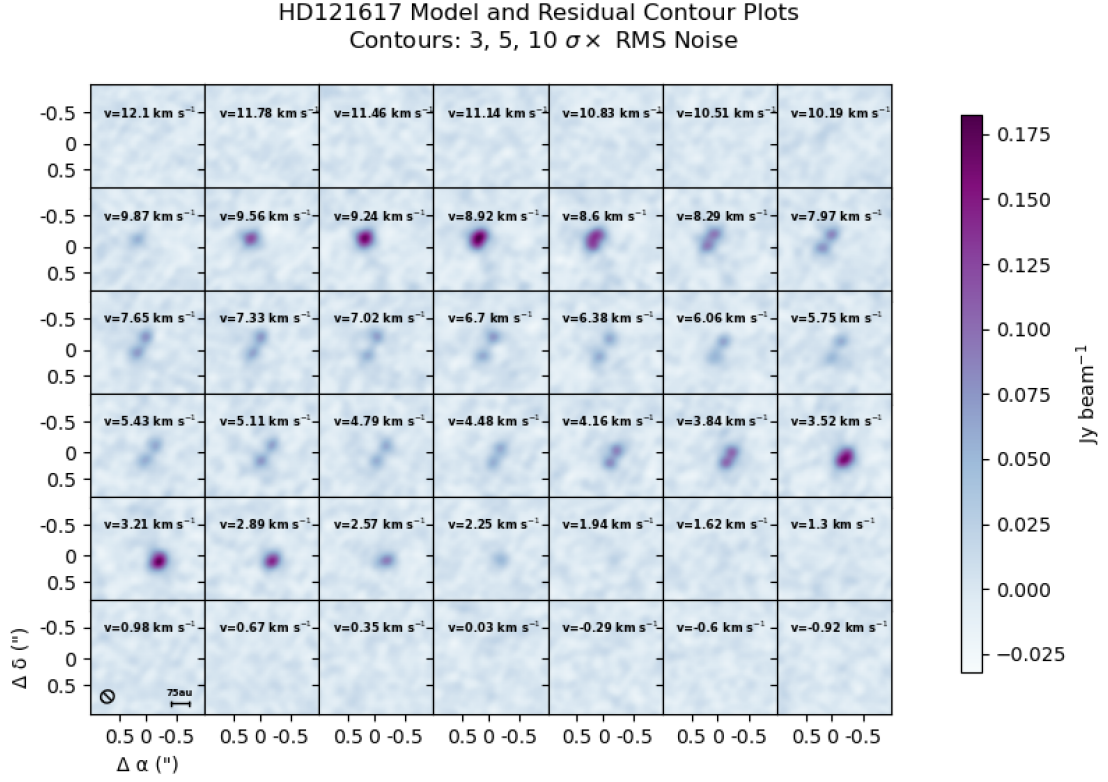


Figure 3.1: HD121617 produced using ALMA data. The RMS noise is 0.0069 Jy beam^{-1} . The solid contour lines demarcate residuals at intervals of 3, 5, and 10 $\sigma \times$ RMS noise. The color bar depicts the intensity of emission. The LSRK velocity of each channel is also provided in km s^{-1} . Overall the residuals are noise-like implying good fit between the data and the model.

emission. In other words it sums the brightness of the CO(2-1) emission across all of our channel maps to produce one image. Mathematically, the moment 0, or integrated value of the spectrum, is defined as:

$$M_0 = \Delta v \Sigma I_i$$

where I_i is the i th pixel of the spectrum, v_i is the coordinate of the i th pixel (Lopez et al. 2014). From 3.2 it's clear that the emission is maximised in a ring-like region around the star and rapidly declines as we leave this region.

Using the moment 0 map we draw 2σ contours around the disk to derive an integrated flux, 1.40 ± 0.06 Jy km s $^{-1}$. We also use moment 0 map to measure the diameter of the major and minor axes, 1.8165" and 1.322" respectively. We use the major axis in combination with the distance value from the *Gaia* database to derive a disk diameter of 88.75 au.

Moment 1 maps allow us to gauge the direction of orbit of the gas around HD121617 via Doppler effect calculations. Doppler shifts are changes in the observers wavelengths of a source. The orbit of the CO gas around HD121617 redshifts, or elongates, the wavelengths of the gas moving away from the observer. In contrast, the wavelength of the gas moving towards the observer is blue shifted, or shortened. Moment 1 maps are intensity weighted velocity figures, where the magnitude of the velocity in any given region is weighted according to the intensity of the emission in this region. Mathematically, moment 1 maps, or intensity weighted coordinate figures, are used to gauge velocity fields via:

$$M_1 = \frac{\Sigma I_i v_i}{M_0}$$

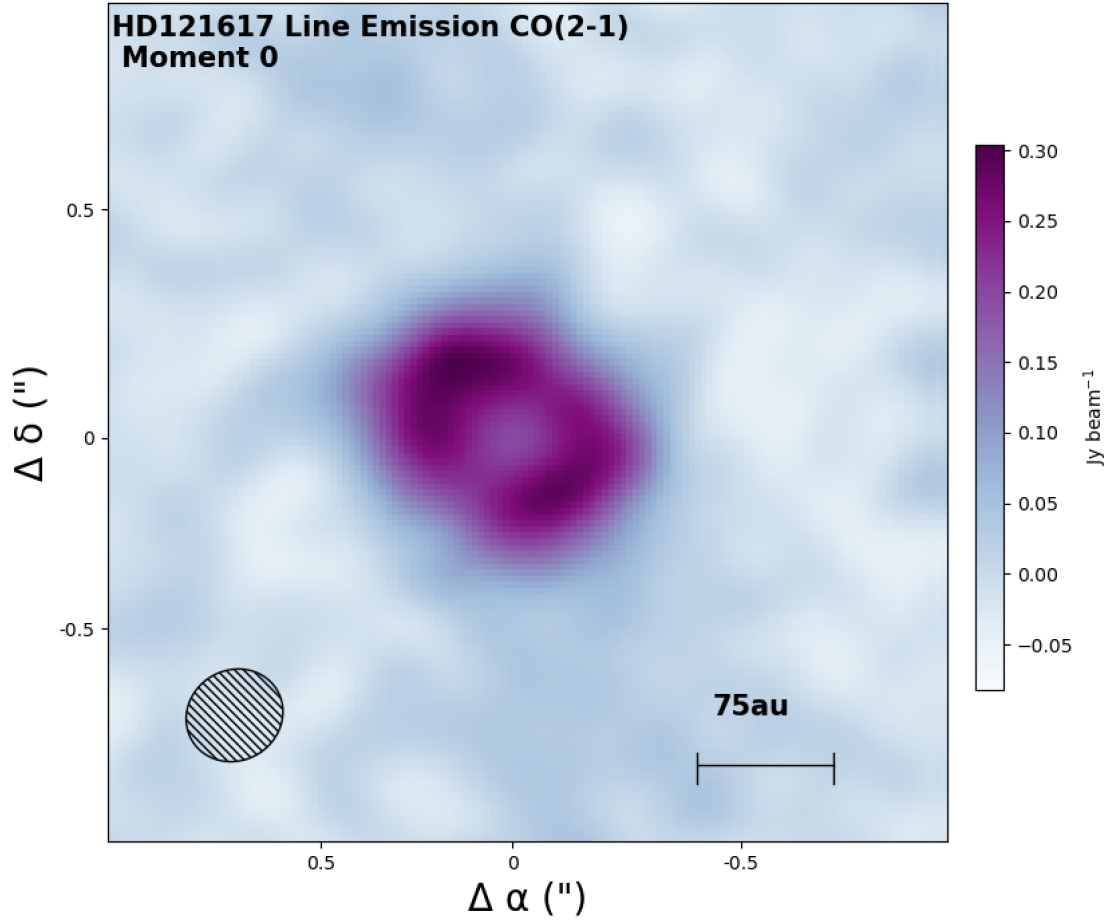


Figure 3.2: A moment 0 map of the CO(2-1) emission. The color bar depicts intensity as a function of color where darker shades represent high intensity of CO emission. The black bar at the bottom right of the panel indicates 75 au scales. The ellipse at the bottom left hand corner depicts the synthesized beam, or effective angular resolution of our observations.

	Left Peak: 8.92 km s ⁻¹	Right Peak: 3.52 km s ⁻¹
Data	309.0 mJy	306.0 mJy
Model	281.0 mJy	279.0 mJy
Residual	28.18 mJy	32.73 mJy

Table 3.1: Flux densities and LSRK velocities corresponding to the peaks in 3.4.

From the 3.3 we notice the emission is red shifted, or moving away from the observer in the northwestern side of the disk, while it's blue shifted, or moving towards the observer, on the southeastern side of the disk ¹.

Finally, we also produce a spectrum plot comparing the data, model, and residuals, 3.4 and observe faithful reproduction of the data. The velocity and flux density associated with the peaks in the data, model, and residuals are summarized in 3.1. Using the spectrum plots we also measure of a full-width-half-max of 6.985 km s⁻¹.

The double-peaked structure is characteristic of Keplerian rotation (the “butterfly wing” pattern that we see in the channel maps 3.1). If you compare 3.1 and 3.4, you can see that the brightest channels in 3.1 correspond to the brightest peaks in the 3.4. The wings of the line reflect the highest-velocity emission, which comes from gas close to the star (because of Kepler’s laws, material close to the star orbit faster). This gas covers a small area on the sky, which makes it faint. The center of the line (halfway between the two peaks) is probing the minor axis of the disk, where the material is moving perpendicular to the observer’s line of sight and therefore has zero rotational shift (no redshift or blueshift). The brightest channels are the intermediate velocities that look like butterfly wings: in these channels, we observe emission coming from a large area of the disk surface, which contributes to brighter emission.

¹To learn about higher order moment maps refer to:
<https://casa.nrao.edu/docs/casaref/image.moments.html>

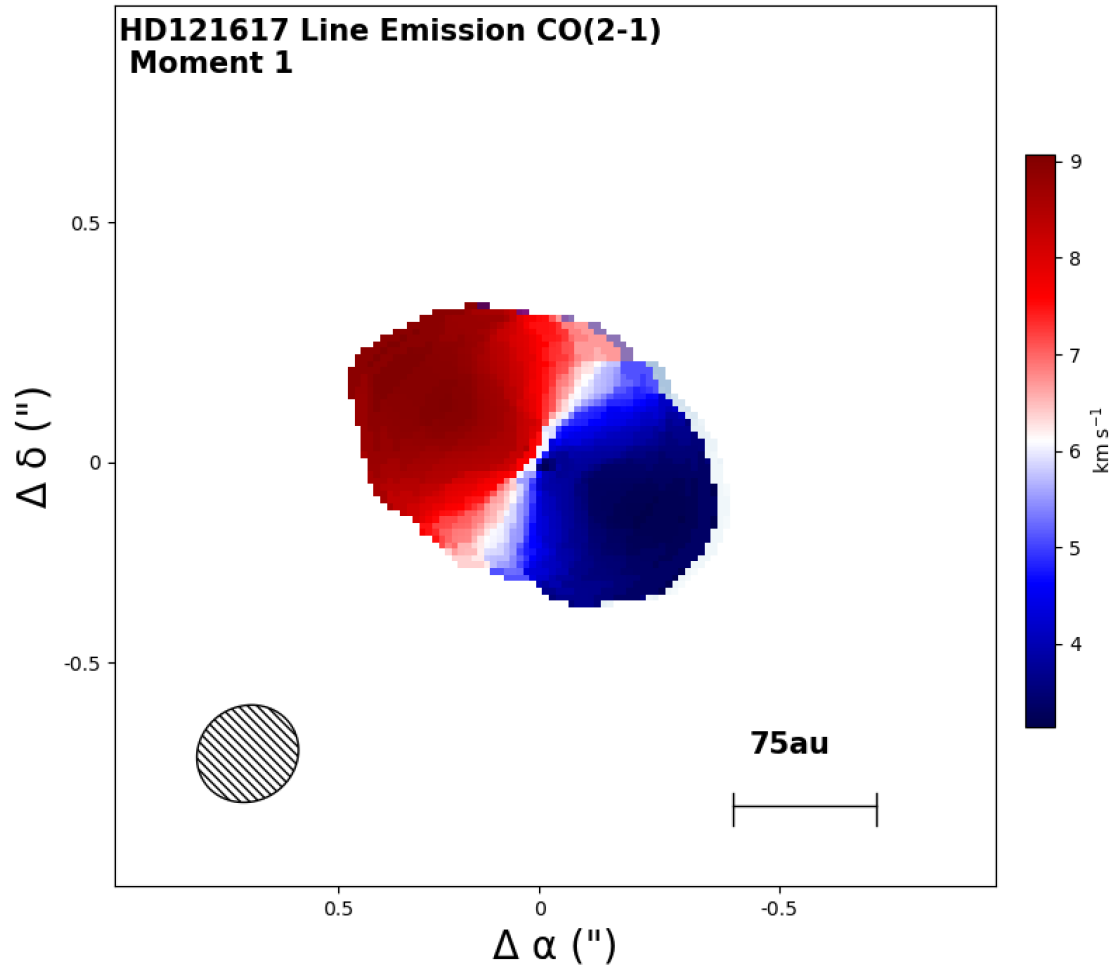


Figure 3.3: A moment 1 map of the CO(2-1) emission. The color bar depicts the gas where blue depicts gas moving towards the observer (out of the page) and red depicts gas moving away from the observer (into the page). The horizontal axis depicts the right ascension offset from the center of the source in arcseconds. The vertical axis depicts the declination offset from the center of the source in arcseconds. The black bar at the bottom right of the panel indicates 75 au scales. The ellipse at the bottom left hand corner depicts the synthesized beam, or effective angular resolution of our observations.

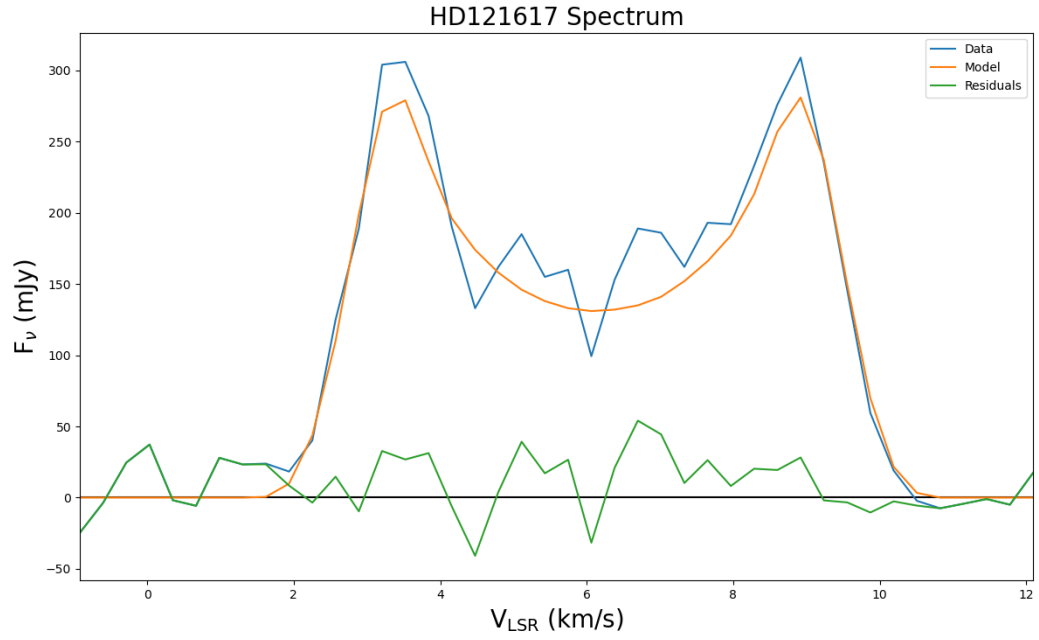


Figure 3.4: A plot depicting the flux density as a function of velocity for the gas in HD121617’s debris disk. The data (blue line) and model (orange line).

Chapter 4

Analysis

In this section we discuss our data preparation and modelling procedure. We begin by discussing the data preparation process through the Common Astronomy Software Applications (CASA) package and the best fit parameters derived from a Markov Chain Monte Carlo (MCMC) process.

Our analysis begins with preparation of the ALMA data sets in CASA. We export our visibilities as fits files, correct the weight of the visibilities, and begin the fitting procedure. The fitting procedure begins by generating parameter values using affine-invariant MCMC. We then create a model disk using the parameters generated from MCMC and perform radiative transfer calculations. We then use Galario (Tazzari et al. 2018) to compute synthetic visibilities. Finally, we compute a χ^2 between the model predictions and the observed visibilities. We describe the results of our analysis and give the best-fit parameters with posteriors in section 4.4.

4.1 Preparation of ALMA Data Set

We time averaged the data so that the file size of the visibilities would be minimized thereby decreasing the run time of the analysis. Observations over time provide us with spatial information about our source. The spatial information results from Earth rotation aperture synthesis. Time averaging helps us determine

the amount of time we can safely average the data without decreasing angular resolution. We time averaged our data using the method described in the Essential Radio Astronomy textbook (James J. Condon and Scott M. Ransom) which compares the time intervals with the angular resolution of the observations:

$$\frac{2\pi\Delta t}{P} \approx \frac{\Delta t}{1.37 * 10^4 s} \ll \frac{\theta_s}{\Delta\theta}$$

where Δt is the time averaging parameter, θ_s is the angular resolution or synthesized beam, and $\Delta\theta$ is the field of view or primary beam size. We gathered the necessary quantities from the header of our visibilities and calculated a timebin of 25.0 seconds. The cleaned channels was converted to a fits file using the `exportfits`.

We correct the statistical weights because there is a known problem with the statistical weights of the visibilities in ALMA data sets. We decide to recompute the weights by calculating the variance of neighboring visibilities following the procedure described in Flaherty et al. (2015b). We then begin fitting our model parameters using affine-invariant MCMC.

4.2 An Introduction to MCMC

Here we discuss Markov Chain Monte Carlo (MCMC) the tool we use to characterize the dynamical masses and their uncertainties. The information below primarily draws on the work presented by Foreman-Mackey publication in 2013 (Foreman-Mackey et al. 2013).

We use the affine-invariant variation of MCMC when producing final models of these systems as it allows us to efficiently explore degeneracies within N-dimensional parameter space.

4.2.1 Background and Vocabulary

1. **Markov Chain** a sequence of steps (or actions) of length n whose $n + 1$ step is only based on the probabilistic outcomes of the n^{th} step; in our code these “steps” reflect our parameters varying over time
2. **Monte Carlo** describes a wide variety of algorithms whose common feature is using randomly generated numbers to explore the impact of randomness or variability on a calculation
3. **Chi-squared** a statistical metric that allows us to quantify the difference between our model and the observations. The formula is as follows:

$$\chi^2 = \sum_{i=0}^{\infty} \chi_i^2 = \frac{(Observed_i - model_i)^2}{\sigma^2}$$

where sigma here is our uncertainty.

4. We utilize any MCMC algorithm to attain estimates of the coefficients associated with a **target function**. This target function, is one that the coder/scientist chooses under the belief that it is optimal in modeling the behavior of some phenomenon (in our case, a function that best describes the shape of a disk in Keplerian rotation around a star).
5. **Walker** we can think of a walker as an entity that possesses values for each of our parameters $w = (p_1, p_2, \dots, p_n)$. These walkers explore the parameter space for each of the parameters in the model, updating their p_i 's as they do.
6. **Walker Position** each walker position is described by a complete set of

values for all of the parameters or variables in the model. These positions are updated, iteratively, as we cycle through the full set of parameters.

7. **Observed data** in our case, each data point is the real or imaginary component of a single complex visibility
8. **Inprobs function** $-\chi^2/2$; used to compare observed results with the model. The probability function,

$$e^{-(\chi^2)/2}$$

.

9. **Priors** functions that take into account prior knowledge of a parameter. Parameters in a model can be constrained using literature estimates. For these constrained parameters, generally, Gaussian priors are constructed such that their mean and standard deviation are sourced from the literature. For those parameters without literature constraints priors, uniform priors are constructed, representing a range of values that are physically possible. These priors determine the domain walkers explore.

4.2.2 Modeling HD121617's Debris Disk

Affine-Invariant MCMC

Affine-Invariant MCMC uses an ensemble Markov Chain. An ensemble Markov Chain $\overrightarrow{X(t)}$ is a group of L walkers that is evolved by moving one walker at a time. Each step consists of one cycle through all L walkers, X_k in the ensemble. We consider one step of the ensemble Markov Chain:

for $k = 1, \dots, L$

update: $X_k(t) = X_K(t + 1)$

In each step, walker positions are updated using the current positions of the remaining $L - 1$ walkers. These remaining $L - 1$ walkers form the complementary ensemble. The complementary ensemble is used to propose a new value of X_k using a stretch move. In a stretch move, walker X_k uses one complementary walker in the complementary ensemble to generate new values for the model parameters also known as the candidate values. The candidate values are generated by proposing a step along a line (in L dimensional space). The operation $\overrightarrow{X}(t) = \overrightarrow{X}(t + 1)$ using one stretch move per walker is given by:

for $k = 1, \dots, L$

1. choose a random walker X_j from the complementary ensemble
2. generate candidate values by creating a line between X_j and X_k and select parameter values that lie along this line
3. accept and update walker values or reject candidate values

Visually, the stretch move is depicted in 4.1 Goodman & Weare (2010). The main advantage of the stretch move is that it leverages the information in the complementary ensemble to update the model parameters in each walker. The candidate values are then accepted or rejected using the chi-squared metric. Another advantage of affine-invariant MCMC is that it allows for the exploration of degenerate parameter spaces because it varies all parameters simultaneously along

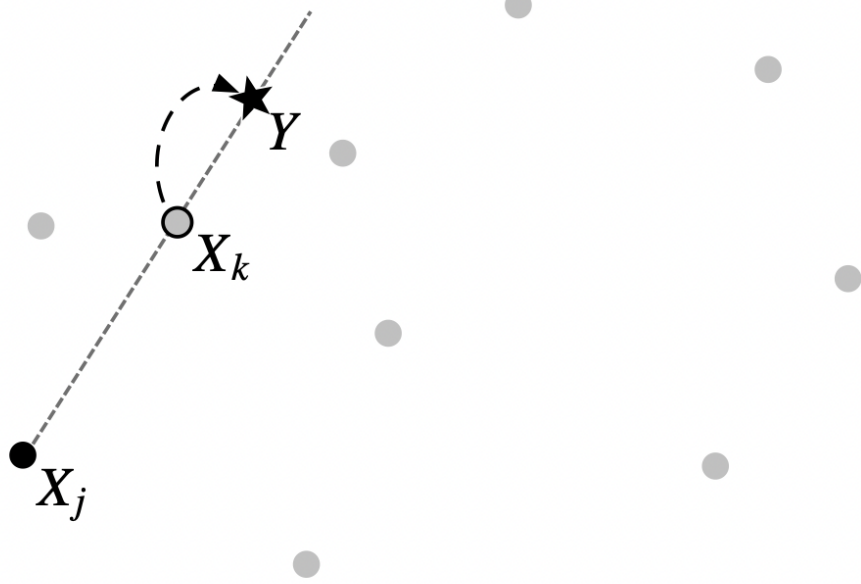


Figure 4.1: A stretch move. The light dots represent the walkers not participating in this move. The proposal is generated by stretching along the straight line connecting X_j to X_k . This figure is from Goodman & Weare (2010).

lines that connect walkers. This is different from other MCMC algorithms, such as Metropolis Hastings, which varies one parameter at a time and thus runs greater risk of being trapped in local minima. To explore the parameter space, we utilized the Python package `emcee` (Foreman-Mackey et al. 2013) which implements the affine-invariant MCMC (Markov Chain Monte Carlo) algorithm described in (Goodman & Weare 2010). MCMC algorithms sample parameter space such that the distribution of samples within a region is proportional to its probability density. This sampling is done using walkers to explore the parameter space yielding best-fit parameters. These walkers traverse N -dimensional space, where N is the number of parameters, adjusting the values for each of the parameters in the model. Affine-invariant MCMC algorithms explore parameter space by accepting (or rejecting) walker movements. Proposed moves are always accepted if they

result in a better fit to the data, but sometimes they are accepted even if the fit is slightly worse. The probability function is compared with a random variable to ensure that the frequency with which walkers move around the parameter space is proportional to the likelihood of the corresponding parameter values.

For an estimate of the total number of samples generated by an MCMC run you simply multiply the number of walkers by the total number of steps. For example, in our procedure we utilized 52 walkers over 4000 steps, so we expect a total of 208,000 samples. The number of samples generated is independent of the number of parameters that are included in the modeling. Thus if we are modeling N parameters, the walkers take one step across N -dimensional space to produce a new candidate sample.

The number of walkers needs to be at least two times the number of parameters. We selected 52 walkers because this would allow optimal use of our computational resources while following the walker-parameter ratio. Some of the samples are regarded as burn-in which are cleaved from the posterior distributions. As mentioned, our walkers traversed parameter space for 4000 iterations. The general rule is to have roughly 10^5 samples after burn-in. We evaluated by eye where the $\ln\text{prob}$ values and parameter values for different chains leveled off to a constant value. We discarded the first 1100 iterations leaving us with a sample size of 150,800.

4.3 Disk Object, Radiative Transfer, and Synthetic Images

We use Flaherty et al. (2015b) ray tracing code ¹ to generate model images. The disk structure is modelled via a few basic equations. The model uses parametric forms of the temperature and density structure that represent protoplanetary disks a self similar density distribution Flaherty et al. (2015b). We also assume that the disk is vertically isothermal because the dust in these disks is optically thick and that the $\text{CO}/\text{H}_2 = 10^{-4}$.

$$T_{atm} = T_{atm0} \left(\frac{r}{150au} \right)^q$$

$$\Sigma_{gas}(r) = \frac{M_{gas}(2 - \gamma)}{2\pi R_c^2} \left(\frac{r}{R_c} \right)^{-\gamma} \exp \left[- \left(\frac{r}{R_c} \right)^{2-\gamma} \right]$$

where T_{atm} is the atmosphere temperature normalization defined at a radius of 150 au, r is the radial position in the disk, q is the temperature radial power law index, σ_c is the surface density profile, R_c is the disk critical radius, M_{gas} is the disk gas mass, and γ is the radial direction power law index of the surface density.

The volume density is calculated assuming hydro-static equilibrium based on the specified surface density and temperature structure.

$$-\frac{\partial \ln \rho}{\partial z} = \frac{\partial \ln T}{\partial z} = \frac{1}{c_s^2} \left[\frac{GM_* z}{(r^2 + z^2)^{3/2}} \right]$$

$$c_s^2 = \frac{k_B T}{v m_h}$$

where the mean molecular weight $v = 2.37$, ρ is the volume density, T is the

¹Kevin Flaherty's Github: <https://github.com/kevin-flaherty>

temperature, M_* is the mass of the star, z is the vertical position in the disk, c_s is the sound speed, k_B is Boltzmann's constant, and m_H is the mass of hydrogen. The velocity of the disk is Keplerian motion, with corrections for the height above the mid-plane and the pressure gradient.

$$\frac{v_\phi^2}{r} = \frac{GM_* r}{(r^2 + z^2)^{3/2}} + \frac{1}{\rho_{gas} \frac{\partial P_{gas}}{\partial r}}$$

where P_{gas} is the pressure from the gas and v_ϕ is the systemic velocity.

Finally, we perform radiative transfer calculations that account for the viewing geometry and distance to disk. This computation is needed to project the disk object onto the sky. We follow the procedure described in Flaherty et al. (2015b). Once we create the disk object, we calculate the flux through the disk, where the line intensity is given by:

$$I_\nu = \int_0^\infty S_\nu(s) \exp[-\tau_\nu(s)] K_\nu(s) d\nu$$

where s is the linear coordinate along the line of sight increasing outward from the observer, $K_\nu(s)$ is the absorption coefficient, and $S_\nu(s)$ is the source function. The optical depth is given by:

$$\tau_\nu(s) = \int_0^s K_\nu(s') ds'$$

For simplicity, our calculations assume Local Thermodynamic Equilibrium (LTE) allowing us to approximate the level populations by the Boltzmann equation and the local gas temperature and the source function by the Planck function.

Description of Disk Parameters of HD121617's Disk	
Parameter	Description
$\log(M_*) (M_\odot)$	dynamically measured mass of HD121617's debris disk
i (degrees)	the tilt of the orbital plane of HD121617's debris disk relative to the observers line of sight
R_{in} (au)	inner radius cutoff in the disk surface density
R_c (au)	critical radius describes the power law drop-off of surface density
q	temperature radial power law index
T_{atm} (K)	atmosphere temperature
PA (degrees)	position angle, the angle measure from the north through the east
$\log(\text{Disk mass}) (M_\odot)$	the mass of gas in HD121617's disk
p	surface density radial power law (Σr^{-p} for $r < R_c$)
v_{sys} (km s $^{-1}$)	the LSRK velocity of HD121617
$\Delta\alpha$ (")	the offset in right ascension
$\Delta\delta$ (")	the offset in declination

Table 4.1: Description of Disk Parameters.

4.4 Best Fit Parameters

Once a synthetic image is created using the parameter values sampled from MCMC and the radiation transfer code, we then use Galario (Tazzari et al. 2018) to translate the model images into model visibilities. Finally, we compare the model visibilities to the observed visibilities from the ALMA data. The quality of fit for each step is measured using the chi-square (χ^2) metric.

Our study models 12 parameters associated with HD121617's disk: dynamical mass of HD121617 (M_*), inclination (i), inner radius (R_{in}), critical radius (R_c), temperature radial power law index (q), atmosphere temperature (T_{atm}), position angle (PA), disk gas mass (M_{disk}), surface density power law (p), and LSRK systemic velocity of HD121617 (v_{sys}), offset in right ascension ($\Delta\alpha$), and offset

Best Fit Parameters of HD121617			
Parameter	Median Value & Uncertainties	Best Fit	Priors
$\log(M_*) (M_\odot)$	$0.2^{+0.005}_{-0.005}$	0.2	[0.01,100]
i (degrees)	$46.5^{+0.3}_{-0.5}$	46.5	[0,90]
R_{in} (au)	$54.8^{+0.2}_{-0.9}$	55.6	[1,100]
R_c (au)	85.0^{+13}_{-9}	78.5	[0,1000]
q	$-0.03^{+0.13}_{-0.14}$	-0.30	[-5,5]
T_{atm} (K)	46.0^{+5}_{-6}	36.5	[0,500]
PA (degrees)	$59.7^{+0.3}_{-0.2}$	59.5	[0,360]
$\log(\text{Disk mass}) (M_\odot)$	$-4.0^{+0.09}_{-0.08}$	-4.1	[-6,-2]
p	$0.5^{+0.4}_{-0.3}$	-0.09	[-4,4]
v_{sys} (km s ⁻¹)	$5.979^{+0.005}_{-0.005}$	5.981	[5.8,6.8]
$\Delta\alpha$ (")	$0.2818^{+0.0025}_{-0.0018}$	0.0290	[-2,2]
$\Delta\delta$ (")	$-0.107^{+0.002}_{-0.002}$	-0.1071	[-2,2]

Table 4.2: Best-fit parameter values along with median values and priors.

in declination ($\Delta\delta$). Table 4.2 lists best-fit values for each parameter, along with the median values with uncertainties derived from the 16th and 84th percentiles of the posterior distribution for each parameter. The boundaries on the uniform priors are given in the final column. Table 4.1 gives a description of each of the parameters that we modeled.

All of the disk parameters were sampled linearly with a uniform distribution with the exception of the star mass and dust mass, which were sampled logarithmically. Our parameters were bounded by priors that were physically reasonable. The data and residual channel maps corresponding to our best-fit parameters are presented in figure 3.1. The residual contours in figure 3.1 are noise-like implying close agreement between the model and the data.

The spectrum plot is presented in figure 3.4. On the horizontal axis we have the LSRK velocity centered at the frequency of CO(2-1) emission. On the vertical axis we have the flux density of the gas emission in the disk. The model (orange

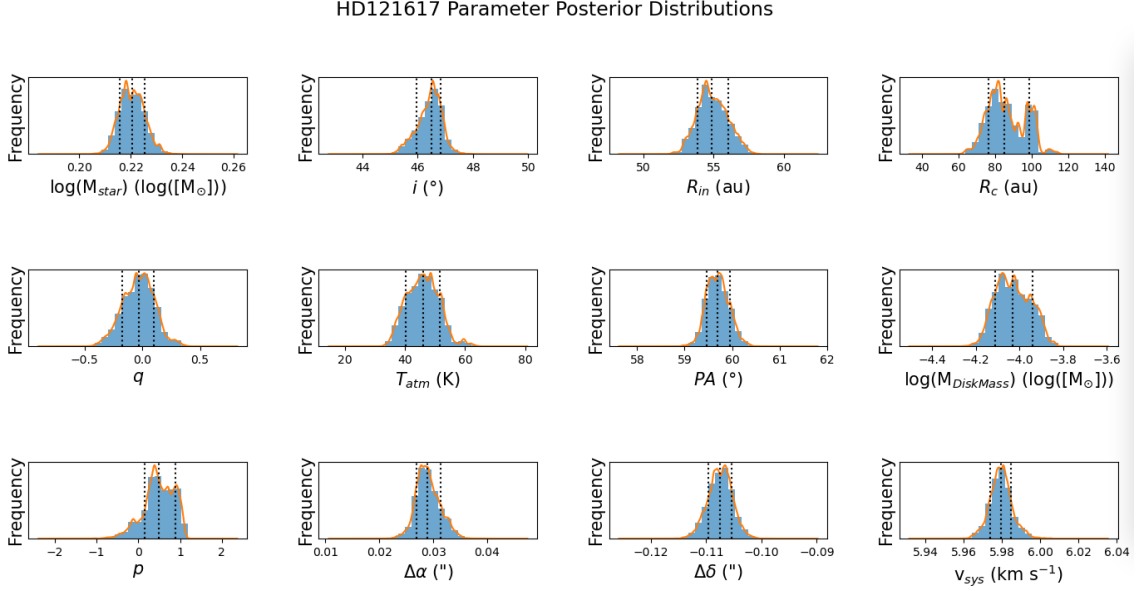


Figure 4.2: Kernel density estimate of the posterior probability distribution for the MCMC modeling runs. The central line represents the median (best-fit) values while the left and right lines represent the 16th and 84th percentiles.

line) represents the flux density present in the synthetic images constructed by the radiative transfer code (Flaherty et al. 2015b). The residuals here are defined as the difference $data - model$. We observe close agreement between the data and the model. We determined the significance of the residuals by comparing the peak flux density in the residuals, $0.0273 \text{ Jy beam}^{-1}$, to the peak flux density in the data, $0.1823 \text{ Jy beam}^{-1}$, and the model, $0.1770 \text{ Jy beam}^{-1}$, in MIRIAD. The residual spectrum is noise-like, indicating good agreement between the model and data.

Finally we also present posterior distributions in figure 4.2. We observe that most parameter distributions are Gaussian-shaped.

Chapter 5

Discussion

This chapter will consider the implications of the results in the context of the literature. We begin by considering our best-fit results for the disk parameters in the context of the literature. We then discuss the development and use of an in house code to download and plot stellar evolution tracks and isochrones from the MIST database (Dotter 2016; Choi et al. 2016; Paxton et al. 2011, 2013, 2015) which is based on the MESA stellar evolution code Paxton et al. (2011, 2013, 2015, 2018, 2019); Jermyn et al. (2023). The third section reviews the history and process of attaining dynamical mass measurements. The final section of this chapter will compare the estimated masses of HD121617 derived from dynamical to those in the literature.

5.1 Comparison of Best Fit Parameters with the Literature

5.1.1 Millimeter Observations (ALMA) of HD121617

The current paradigm of circumstellar disk evolution is that gas-rich disks evolve into gas-poor debris disks composed of second generation dust. However, literature data relating to the study of dust-rich debris disks around young A-type stars within 150 pc, measure a CO detection rate of 11/16 above a $^{12}\text{CO } J = 2-1$

line luminosity threshold of $1.4 \times 10^4 \text{ Jy km s}^{-1} \text{ pc}^2$ (Moór et al. 2017). This high incidence implies that the presence of CO gas in bright debris disks around young A-type stars is likely more a rule than an exception. To better understand the evolution of gas in these systems Moór et al. (2021, 2017) studies the incidence and physical parameters of the molecular gas component of A-type stars.

Moór et al. (2017) observes HD121617, among other target and probes for CO $J = 2-1$ lines. Moór et al. (2017) produces zeroth moment maps of ^{12}CO where they measure an integrated flux density of $1.27 \pm 0.13 \text{ Jy km s}^{-1}$ (vs, our $1.40 \pm 0.06 \text{ Jy km s}^{-1}$). These measurements are consistent with our own within the 0.9σ level. These measurements place HD121617 among the brightest debris disks in the literature. Moór et al. (2017) also produces spectrum plots allowing us to estimate the LSRK velocity of HD121617. (Moór et al. 2017)’s spectrum plots reveal a $v_{sys} = 6.00 \text{ km s}^{-1}$ (vs. our $v_{sys} = 5.979_{-0.005}^{+0.005} \text{ km s}^{-1}$). Rebollido et al. (2018) also reports a systemic $v_{sys} = 7.8 \pm 1.6$, which is in agreement with our measurements within the 1.1σ level. The discrepancy with Rebollido et al. (2018) and those of Moór et al. (2017) and our own is attributed to their use of Ca and Na emission lines. (Moór et al. 2017) also reports an inclination and position angle both of which are consistent with our measurements within the 0.7σ and 0.9σ levels, respectively.

In another study, (Smirnov-Pinchukov et al. 2022) uses ALMA data to survey the molecular content of four gas-bearing debris disks (HD121617 included) and compares them to the primordial disks around Herbig Ae stars. Herbig Ae stars span $2-10M_{\odot}$ and are free of circumstellar envelopes. This absence of these envelopes allows for unobscured and direct observation of the circumstellar disks around these stars.

(Smirnov-Pinchukov et al. 2022) also measures an inclination (in degrees) of

43.9 ± 3.0 (vs our $46.5^{+0.3}_{-0.5}$) which is consistent with our measurements within the 0.9σ level. (Smirnov-Pinchukov et al. 2022) also reports of a position angle (in degrees) of 53.5 ± 4.0 (vs our $59.7^{+0.3}_{-0.2}$) which is consistent with our measurements within the 1.5σ . This study also reports an inner gas radius of 50 au (vs our $54.8^{+0.2}_{-0.9}$).

5.1.2 Scattered Light Observations of HD121617

In the literature, most of the studies performed on HD121617 are done using the ALMA to probe the disk morphology at mm wavelengths. Perrot et al. (2023) presents scattered light observations of the disk.

Millimeter and scattered light observations provide complementary information by tracing different dust grain sizes that respond to different physical mechanisms (i.e., small grains trace by scattered light are sensitive to radiation pressure, stellar winds, and ISM forces, whereas mm grains primarily trace gravitational potential).

To perform a morphological analysis of the SPHERE observations, Perrot et al. (2023) used the radiative transfer code Debris DIks Tool, DDiT, (Olofsson et al. 2020) to create synthetic models of the debris disk. Then the DDiT was used with an MCMC code based on the **emcee** (Foreman-Mackey et al. 2013). Though (Perrot et al. 2023) uses the same sampling methods as our study, the underlying physics encoded in their synthetic models differ from the ones we used. For example, DDiT treats the dust density distribution of the disk in the following way:

$$n(r, z) \propto \left[\left(\frac{r}{r_0} \right) + \left(\frac{r}{r_0} \right)^{2\alpha_{out}} \right]^{1/2} \exp^{-z^2/2h^2}$$

where n is the dust grain volumetric density, r as the radial direction, z as the

vertical direction, r_0 as the reference radius of the disk, α_{out} as the outer coefficients of the slope of the dust density distribution, and h the scale height of the disk.

(Perrot et al. 2023) modeling also treats the case of a non-eccentric circular debris disk, defining the reference radius as:

$$r_0(\gamma) = \frac{a(1-e)^2}{1+e\cos(\omega+\gamma)}$$

where a is defined as the semi-major axis, e the eccentricity, w the pericenter, and γ the azimuthal angle of the disk at r_0 . Finally, to treat polarized light they also implement a polarized scattering phase function using the Henyey-Greenstein approximation (Henyey & Greenstein 1941):

$$f_{HG} = \frac{1 - \cos^2(\theta)}{\cos^2(\theta)} \frac{1}{4\pi} \frac{1 - g^2}{(1 + g^2 - 2g\cos(\theta))^{3/2}}$$

where g is the scattering anisotropy of the dust and θ is the scattering angle. Perrot et al. (2023) models the semi-major axis, inclination, position angle of the major axis with respect to the north, anisotropic scattering coefficient, inner and outer slope of the power law distribution of dust density, eccentricity and pericenter. Of these parameters, we share similar best fit values for the inclination as Perrot et al. (2023) reports θ_{incl} (degrees) 43.4 ± 0.8 (vs $46.5^{+0.4}_{-0.5}$); these results are consistent with our measurements within the 3.4σ level. (Perrot et al. 2023) also reports a PA of 60 ± 0.9 (vs $59.7^{+0.3}_{-0.2}$) which is consistent with our measurements within a 0.3σ level. Both position angle measurements are relative to the major axis in degrees east of north.

5.2 Plotting Stellar Evolutionary Tracks and Isochrones

We developed code that downloads and plots stellar evolution tracks and isochrone curves with the intention of investigating the discrepancies between dynamical and photometric mass measurements of young, gas-rich, low mass stars.

The idea of using gas-bearing circumstellar disks to measure dynamical masses is first referenced in the literature during the 1980s and 1990s (Ono & Shimaoka 1984; Mathieu et al. 1994). During this time, however, the dynamical mass measurement techniques were limited by high uncertainties in distance measurements. It was not until the advent of *Gaia* that astronomers would be able to measure distances to sources with much higher precision. Given the dependence that dynamical mass measurement techniques have on the distance to stellar objects, *Gaia*'s more precise measurements also allowed for more precise dynamical mass measurements.

Many of the dynamical masses measured since the launch of *Gaia* in 2013 are in agreement with fiducial stellar models. For example Boyden & Eisner (2023) studies 20 protoplanetary, pre-MS, disk systems and finds agreement between the dynamical masses and stellar evolutionary models. In another study, Sheehan et al. (2019) estimates the mass of pre-MS binary system and also finds agreement with stellar evolutionary models. Similar results were produced in Czekala et al. (2016). However (Pegues et al. 2021)'s study of M-dwarfs with protoplanetary disks showed significant discrepancies between the dynamical masses and spectroscopic/photometric estimates. This indicates that, for at least some categories of stars, the fiducial models need to be improved. The dynamical mass measurements can provide important insight on the performance of fiducial stellar evolutionary models in different stellar regimes. In the event that both mass

measurement techniques agree, the astronomical community will have developed a procedure that verifies its models from two distinct physical approaches. In the more interesting case, both mass measurement techniques do not agree and the astronomical community must question the assumptions made in stellar evolutionary models. We produce HR diagrams for HD121617’s debris disk. In doing so this code will test fiducial stellar models in a largely unexplored stellar regime namely those main sequence, gas-bearing debris disk host stars. In order to attain photometric mass measurements of stars, the luminosity and temperature of a star must be plotted on the HR diagram. Then, using isochrone and evolutionary tracks, we provide a mass constraint on the plotted point. An isochrone in the HR diagram, represented by vertical lines, represents stars of the same age across many different stellar masses. This allows us to compare the temperature and luminosity as a function of stellar age and mass. The evolutionary tracks (EEP), depicted by the black lines in figure 5.1, shows the path a star of a given mass would take through the HR diagram. In our case, the black line in 5.1 represents HR diagram parameter space that is bounded by evolutionary tracks for stars within 1-sigma of our median dynamical mass measurement. The ages we used were gathered from the literature Smirnov-Pinchukov et al. (2022); Pecaute & Mamajek (2016), 16 Myr and 16 ± 2 , respectively. We note that Smirnov-Pinchukov et al. (2022) makes the simplification of quoting the age of the group HD121617 belongs to (UCL), while Pecaute & Mamajek (2016) derives the age based on the star formation history of their sample.

5.2.1 HR Plotting Tool

To study stellar evolution, isochrones and stellar evolutionary tracks are generated using the Modules for Experiments in Stellar Astrophysics (MESA) software. A compilation of the produced tracks is found at the MESA Isochrones and Stellar Tracks (MIST) web page. To best meet the plotting demands of this project, we developed a code that extracts user-specified files from the website and interpolates the data sets.

For the purposes of this study the code interacts with synthetically produced isochrone tracks produced using UBVRI, 2MASS JHKs, Kepler, Hipparcos, Tycho, and *Gaia* data in both $v/v_{\text{crit}} = 0.0$ and $v/v_{\text{crit}}=0.4$ regimes. v/v_{crit} compares the rotational velocity of the star, v , to its critical rotational velocity, v_{crit} . Here the critical rotational velocity is the point where the star begins losing mass along the equator. By introducing these two v/v_{crit} classifications the user can choose the data that best characterizes the rotational velocity of their star of interest. Likewise, we utilize all evolutionary tracks available at the MIST web page, spanning all documented metallicities. The tables from MIST are set up such that there are grouped first by v/v_{crit} (0.0 or 0.4), then metallicity ($[\text{Fe}/\text{H}]$ 0.50 to -4.00), and finally mass (0.1 to 300 M_{\odot}).

The code begins by asking the user for their desired data sets, and then automates the downloading procedure. The user is then asked to specify the mass range for the tracks they would like to plot. The user can plot an evolutionary track spanning 0.01 solar masses to 300 solar masses with precision up to a hundredths of a solar mass. The user is then asked to input the minimum and maximum age for their evolutionary tracks. Here, the age range and precision is determined by data points available in the original data set as it is simply used

to subset the data.

We utilize two-dimensional linear interpolation techniques. Using the user-input lower bound for stellar mass (LMB) we attain the data corresponding the largest stellar mass file less than the LMB (min_{low}), and the data corresponding to the smallest stellar mass file greater than the LMB (min_{high}). After locating these files, we linearly interpolate from min_{low} to min_{high} at steps of 0.01 thereby allowing us to interpolate temperature and luminosity data for stars to a precision of $0.01M_{\odot}$. Let us call the number of 0.01 steps needed to reach min_{high} from min_{low} s . Then, the number of steps k needed to reach the user-input stellar mass from the min_{low} mass file, is used to index linearly interpolated temperature and luminosity data. The temperature and luminosity data were interpolated such that s data points were created between $t_{i,minlow}$ and $t_{i,minhigh}$ and $l_{i,minlow}$ and $l_{i,minhigh}$, once the luminosity l and temperature t arrays from both min_{high} and min_{low} were truncated to the same size. The LMB temperature and luminosity arrays are generated by indexing the k^{th} elements of the interpolated temperature and luminosity arrays.

The code distinguishes itself in that it offers users the capability of producing evolutionary tracks to a precision not already offered by the MIST data base. It interpolates for luminosity and temperature characteristics of stars with precision of up to a hundredth's of a solar mass. We note that a limitation of this code is that the age was not interpolated. Despite this, we believe the code still serves a practical purpose especially because the goal is to precisely constrain the mass of the stars using its location on the HR diagram. Additionally, the data corresponding to the stellar age is very granular, often offering 10 significant digits and precision of at least years.

5.2.2 A Brief History of Dynamical vs Photometric Mass Measurement Techniques

In the literature, (Perrot et al. 2023; Pegues et al. 2021; Hughes et al. 2018; Czekala et al. 2015, 2016; Sheehan et al. 2019; Dutrey et al. 1994; Simon et al. 2000; Dutrey et al. 2003; MacGregor et al. 2017; Ricci et al. 2017; Simon et al. 2017) have done similar studies, deriving dynamical mass measurements of other stellar systems. Though stellar evolutionary models are often used to predict the masses of young stars from observational estimates of the stars luminosities and temperature, doing so is often observationally and theoretically challenging. Observationally, uncertainties in the temperature and luminosities lead to inaccurate models. Theoretically, fiducial stellar evolutionary models do not account for the complex physics that these stars undergo in their maturation. These uncertainties birthed the dynamical mass measurement technique.

Dynamical mass measurements leverage the Keplerian rotation profiles of the disks, observed in molecular line emission to estimate stellar masses. As an example, we refer to derivation below:

If a particle of mass m orbits within a spherical distribution of mass, then the net gravitational force F on it depends only on the mass interior to its position, M_{int} . We can then derive a simple relationship between orbital velocity v at some radius r and the amount of mass interior to that radius: M_{int}

$$F = \frac{GM_{int}m}{r^2} = \frac{mv^2}{r}$$

where G is the gravitational constant. Solving for the velocity as a function of

the radius:

$$v(r) = \sqrt{\frac{GM_{int}}{r}}$$

As previously mentioned, past studies have shown agreement between dynamical masses to stellar evolutionary tracks (Boyden & Eisner 2023; Sheehan et al. 2019; Czekala et al. 2016). However, the literature also reports discrepancy between both methods. Specifically, the dynamical mass measurements both under-predicted the photometric mass measurements by up to 80% (Pegues et al. 2021) and in other studies, over-predicted photometric mass measurement techniques by 30% (Simon et al. 2019). The disagreement between these techniques, especially as it relates to mass estimates for young, low-mass stars, is attributed to inaccurate assumptions of stellar effective temperature, undetected binary, and the absence of magnetic treatment and other physical mechanisms in fiducial stellar evolutionary models (Simon et al. 2019) .

Simon et al. (2019) presents a study on 29 single stars with masses measured to a precision of at least 10%. Their results include 9 updated mass determination and 3 that have not had their dynamical masses published before. They reach their estimates by placing their dynamical mass estimates on the HR diagram to compare them with stellar evolutionary tracks that treat magnetic fields and stellar evolutionary tracks that do not treat magnetic fields. They find that stellar evolutionary models that treat magnetic fields are in much better agreement with their dynamical mass estimates with an average difference of $0.01 \pm 0.02 M_{\odot}$. When comparing the dynamical mass estimates to stellar evolutionary models that do not treat magnetic fields (Simon et al. 2013) finds that differences are greatest for stars in star-forming regions where stellar masses are $< 1.5 M_{\odot}$ and age is < 10 Myr. As a result, this study provides robust way (at least in comparison to stellar

evolutionary models that do not incorporate magnetic fields) of understanding the earliest stages of star and planet formation.

As mentioned previously, (Simon et al. 2019) found that stellar evolutionary models that do not treat for magnetic fields underestimated dynamical mass measurements by about 30%. However, there is now much greater agreement among recent models of pre-main sequence evolution. For example, stellar masses $\geq 0.5 M_{\odot}$ and age > 1 Myr, the models of (Baraffe et al. 2015) Modules for Experiments in Astrophysics, Mesa (Paxton et al. 2015; Choi et al. 2016) and the nonmagnetic models of (Feiden 2016) are in agreement with masses measured using MESA in (Simon & Toraskar 2017).

To further our understanding of the impact that magnetic fields have on stellar mass estimates, (Flores et al. 2022) studies its impact on the young stars. Young stars have magnetic fields that produce hot and cold spots on their surfaces. The hot spots are produced through accretion of circumstellar material (Calvet & Gullbring 1998; Hartmann et al. 2016). Hot spots also result from stellar plagues (extended bright areas or patches on the surface of a star) that form in environments of high magnetic activity (Strassmeier & Ilyin 2009). In contrast, cold spots result when magnetic fields inhibit the transport of energy through convection. This results in localized dark regions (Berdyugina 2005). Though there is substantial research on the photometric effects of star spots, spectroscopic effects have been largely neglected because it is observationally expensive and most evolved stars host weak magnetic fields. This poses an issue especially for studies of low-mass stars with ages much less than 1 Myr to over a Gyr old. Vidotto et al. (2014) found that the average magnetic field value of main sequence stars is thousands of times weaker than those present in young stars. This difference has important implications on the size and temperatures observations of young

stars as they are likely more affected by magnetic fields than their more evolved counterparts. The effects of magnetic fields on stellar temperatures have been studied in Vacca & Sandell (2011); Gully-Santiago et al. (2017); Flores et al. (2019, 2020). This issue is relevant in our study because inaccurate temperature estimates affect the location of the stars in the HR diagram which then skews spectroscopic mass estimates.

5.2.3 HD121617: Dynamical vs. Spectroscopic Mass Measurements

HD121617 is an A1V (Houk 1978) main sequence star, member of the Upper Centaurus Lupus (UCL) association (Hoogerwerf 2000; Gagne et al. 2019), and has an estimated age of 16 ± 2 Myr (Pecaut & Mamajek 2016). *Gaia* reports a median distance of 119.4117 pc with uncertainties derived from the 16th and 84th percentiles, 119.4117 pc and 120.5318 pc, respectively. In the literature, the most recent estimates of stellar parameters referenced by studies of gas-rich debris disks report a luminosity of $L_* = 14.9L_\odot$ (Moór et al. 2017) while (Matrà et al. 2018) estimates $L_* = 17.3L_\odot$. Discrepancies between these two measurements is attributed to their methods; Moór et al. (2017) derives her luminosity from Spectral Energy Distribution (SED) plots while Matrà et al. (2018) uses Monte Carlo techniques to fit for the $R - L_*$ relation. In Rebullido et al. (2018), authors estimated $T_{eff} = 9285K$ spectroscopically using high resolution optical spectra. This measurement is in close agreement with (Smirnov-Pinchukov et al. 2022), who measures a $T_{eff} = 9050$ spectroscopically with ALMA data.

Stellar evolutionary models are often used to predict the masses of young stars using the observational estimates of luminosity and effective temperatures. These

mass estimates are important for understanding not only individual stellar evolution but also entire star forming regions. We use the luminosity and temperature estimates of HD121617 found in *Gaia*'s gaiadr3.astrophysical parameters table¹ as a data point. *Gaia* reports a median $T_{eff} = 9651.733$ K with uncertainties derived from the 16th and 84th percentiles, 9641.973K and 9657.166K respectively. They also report a median $L_{\odot} = 18.83192L_{\odot}$ with uncertainties derived from the 16th and 84th percentiles, 18.691252 L_{\odot} and 18.967817 L_{\odot} respectively. These uncertainties were derived from their MCMC posterior distributions. We also use Zhang et al. (2023)'s catalog of stellar parameters to gauge the metallicity, luminosity, and temperature of HD121617 where he reports a $[Fe/H] = -0.4 \pm 0.4[dex]$, $23.70 L_{\odot} \pm 1.70 \times 10^{-4}$, and $T_{eff} = 10174K \pm 524.1K$. Discrepancies between *Gaia* and Zhang et al. (2023)'s T_{eff} and L_{\odot} is attributed to their methods; where *Gaia* make these measurements using only the spectra from their observations, Zhang et al. (2023) develops their own data-driven model of *Gaia* XP spectra as a function of stellar parameters. The modeling procedure described in Zhang et al. (2023) is complemented by data from 2MASS and WISE photometry allowing them to measure more precise measurements. In this way, Zhang et al. (2023) overcomes important limitations that the astrophysical parameters released in *Gaia* DR3 faced, such as its low-resolution spectra. This plays a crucial role in our analysis because as previously mentioned the effect of magnetic fields on spectroscopic measurements is less obvious in low-resolution spectra.

In 5.1 we compare the dynamical mass measurement (black lines) to the *Gaia* and Zhang et al. (2023) temperature and luminosity estimates. The black lines represent the region in the HR diagram that span stars of mass 1.68 M_{\odot} and 1.72 M_{\odot} across ages of 14 to 18 Myrs. The blue data point towards the top of the

¹<https://gea.esac.esa.int/archive/>

plot represents the temperature and luminosity estimates from *Gaia*. The purple data point represents the temperature and luminosity estimates from Zhang et al. (2023).

Figure 5.1 displays 3 distinct black curves, these of which represent the evolutionary tracks of stars with varying metallicity: the evolutionary track towards the bottom left represents a star of metallicity $[Fe/H] = -0.75$, the more centralized evolutionary track represents a star of metallicity $[Fe/H] = -0.50$, and the evolutionary track towards the bottom right represents a star of metallicity $[Fe/H] = 0.00$. We chose to plot these 3 metallicities to span the metallicity range given by the uncertainties in Zhang et al. (2023)’s database.

5.1 clearly depicts a discrepancy between the dynamical and spectroscopic *Gaia* and Zhang et al. (2023) measurements. Using the mass-luminosity relation

$$L \propto M^{3.5}$$

to estimate the mass of HD121617 we find that the measurements from *Gaia* yield a stellar mass of $2.30M_{\odot}$. This overestimates our dynamical mass measurement by 35%. We repeat the same calculation for Zhang et al. (2023)’s data point via the mass-luminosity relation and find that it overestimates our dynamical mass measurement by 47%.

5.2.4 Explaining the Discrepancies

The uncertainty in the metallicity measurement is $0.4[dex]$ allowing for a metallicity range of 0.00 to -0.80. By varying the metallicity across this range we found that it had a significant impact on the region covered by our dynamical mass measurement. Even after accounting for this metallicity range, we find that

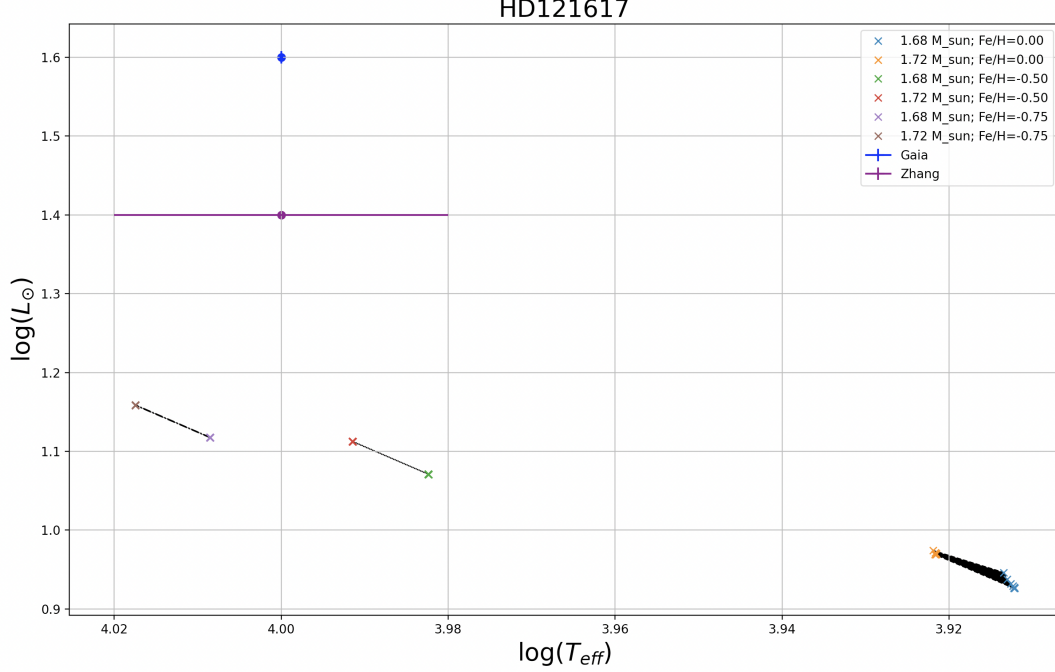


Figure 5.1: Stellar Tracks across stellar effective temperature (T_{eff}) and stellar luminosity (L_*). The tracks spanning the area between the blue and orange crosses follow the 14-18 Myr evolution of stars with masses 1.68-1.72 M_{\odot} . The data points corresponding to the boundaries of the black region were linearly interpolated using the data available in the MESA Isochrones and Stellar Tracks database, MIST (Dotter 2016; Choi et al. 2016). The blue data point marks the placement of HD121617 using the temperature and luminosity measured by *Gaia* while the purple data point marks the placement of (Zhang et al. 2023)’s estimates.

discrepancies between the dynamical mass and *Gaia*’s and Zhang et al. (2023) spectroscopic mass estimates persist.

As previously mentioned, in situations where the dynamical mass measurements did not agree with stellar evolutionary models, the literature turns to the lack of treatment of magnetic fields as a culprit. We acknowledge that this is not the case here as MESA treats for magnetic activity. Further, magnetic activity is less of an issue with HD121617 in particular because it is a main sequence star and has thus surpassed much of the magnetic activity that stars experience in their pre-MS phases.

Chapter 6

Conclusion

6.1 Summary and Future Work

This work presents the 12CO emission of HD121617’s debris disk. We used ALMA data to investigate the dynamics of the gas and produce a dynamical mass estimate to compare it with stellar evolutionary models. This disk is well-suited for radiative transfer modeling of the Keplerian motion of the gas in the disk. We pair the radiative modeling of the disk with an affine-invariant MCMC methods, as described in Goodman & Weare (2010).

We used Flaherty et al. (2015b)’s radiative transfer code, DISKMODEL3, to fit the ALMA 12CO channel maps for HD121617. With new, precise distance measurements for this source, we are able to make high precision direct measurements of HD121617’s mass. The mass measurement is no longer limited by the distance as in previous studies. We find that HD121617 has a mass of $1.70^{+0.02}_{-0.02}$. Comparing with stellar masses estimated using the MESA stellar evolutionary database, we find that our dynamical mass estimate for HD121617 is not in agreement with the model. The large discrepancy for this may be caused due to the large uncertainties on metallicity estimates which has the effect of shifting our dynamical mass estimate through a large region on the HR diagram.

Future studies should leverage the synergy of ALMA, *Gaia*, and detailed ra-

diative transfer disk modeling as this will enable precise mass measurements of dynamical masses for a large number of stars ultimately allowing for the evaluation of our stellar evolutionary models.

6.2 Acknowledgments

This paper makes use of the following ALMA data: 2015.1.01243.S, PI: M. Cure. This research made use of NASA’s Astrophysics Data System. This work used data from the European Space Agency (ESA) mission *Gaia*¹. This research made use of the SIMBAD database operated in CDS, Strasbourg, France. This research made use of the Astropy, a community-developed Python package for Astronomy (Astropy Collaboration et al. 2013, 2018, 2022). This research made use of Pandas (Wes McKinney 2010), NumPy (Harris et al. 2020), and SciPy (Virtanen et al. 2020) libraries.

¹<https://gea.esac.esa.int/archive/>

Bibliography

- 1999, Astronomical Society of the Pacific Conference Series, Vol. 180, Synthesis Imaging in Radio Astronomy II
- Al-Wardat, M. A., Hussein, A. M., Al-Naimiy, H. M., & Barstow, M. A. 2021, Publications of the Astronomical Society of Australia, 38, doi:10.1017/pasa.2020.50
- Andrews, S. M. 2020, ARA&A, 58, 483
- Astropy Collaboration, Robitaille, T. P., Tollerud, E. J., et al. 2013, A&A, 558, A33
- Astropy Collaboration, Price-Whelan, A. M., Sipőcz, B. M., et al. 2018, AJ, 156, 123
- Astropy Collaboration, Price-Whelan, A. M., Lim, P. L., et al. 2022, apj, 935, 167
- Bailer-Jones, C. A. L., Rybizki, J., Fouesneau, M., Demleitner, M., & Andrae, R. 2021, VizieR Online Data Catalog, I/352
- Baraffe, I., Homeier, D., Allard, F., & Chabrier, G. 2015, A&A, 577, A42
- Berdyugina, S. V. 2005, Living Reviews in Solar Physics, 2, 8
- Boyden, R. D., & Eisner, J. A. 2023, ApJ, 947, 7
- Calvet, N., & Gullbring, E. 1998, ApJ, 509, 802
- Carpenter, J. M., Mamajek, E. E., Hillenbrand, L. A., & Meyer, M. R. 2009, ApJ, 705, 1646

- Choi, J., Dotter, A., Conroy, C., et al. 2016, *ApJ*, 823, 102
- Cotten, T. H., & Song, I. 2016, *The Astrophysical Journal Supplement Series*, 225, 15
- Czekala, I., Andrews, S. M., Jensen, E. L. N., et al. 2015, *ApJ*, 806, 154
- Czekala, I., Andrews, S. M., Torres, G., et al. 2016, *ApJ*, 818, 156
- . 2017, *ApJ*, 851, 132
- Dotter, A. 2016, *ApJS*, 222, 8
- Dutrey, A., Guilloteau, S., Prato, L., et al. 1998, *A&A*, 338, L63
- Dutrey, A., Guilloteau, S., & Simon, M. 1994, *A&A*, 286, 149
- . 2003, *A&A*, 402, 1003
- Eggen, O. J. 1983, *MNRAS*, 204, 377
- Feiden, G. A. 2016, in 19th Cambridge Workshop on Cool Stars, Stellar Systems, and the Sun (CS19), Cambridge Workshop on Cool Stars, Stellar Systems, and the Sun, 44
- Flaherty, K., Muzerolle, J., Balog, Z., et al. 2015a, Studying Inner Protoplanetary Disk Structure through its Rapid and Gradual Variability, Spitzer Proposal ID 12090
- Flaherty, K. M., Hughes, A. M., Rosenfeld, K. A., et al. 2015b, *ApJ*, 813, 99
- Flores, C., Connelley, M. S., Reipurth, B., & Boogert, A. 2019, *ApJ*, 882, 75
- Flores, C., Connelley, M. S., Reipurth, B., & Duchêne, G. 2022, *ApJ*, 925, 21

- Flores, C., Reipurth, B., & Connelley, M. S. 2020, *ApJ*, 898, 109
- Ford, E. B. 2005, *AJ*, 129, 1706
- Foreman-Mackey, D., Conley, A., Meierjürgen Farr, W., et al. 2013, emcee:
The MCMC Hammer, Astrophysics Source Code Library, record ascl:1303.002,
ascl:1303.002
- Fujiwara, H., Ishihara, D., Onaka, T., et al. 2013, *A&A*, 550, A45
- Gagne, J., Roy-Loubier, O., Faherty, J. K., Doyon, R., & Malo, L. 2019, VizieR
Online Data Catalog, J/ApJ/860/43
- Goodman, J., & Weare, J. 2010, *Communications in Applied Mathematics and
Computational Science*, 5, 65
- Greaves, J. S., Holland, W. S., Matthews, B. C., et al. 2016, *MNRAS*, 461, 3910
- Guilloteau, S., & Dutrey, A. 1998, *A&A*, 339, 467
- Gully-Santiago, M. A., Herczeg, G. J., Czekala, I., et al. 2017, *ApJ*, 836, 200
- Harris, C. R., Millman, K. J., van der Walt, S. J., et al. 2020, *Nature*, 585, 357
- Hartmann, L., Herczeg, G., & Calvet, N. 2016, *ARA&A*, 54, 135
- Hauschildt, P. H., Allard, F., & Baron, E. 1999, *ApJ*, 512, 377
- Hoogerwerf, R. 2000, *MNRAS*, 313, 43
- Houk, N. 1978, Michigan catalogue of two-dimensional spectral types for the HD
stars

- Hughes, A. M., Duchêne, G., & Matthews, B. C. 2018, *Annual Review of Astronomy and Astrophysics*, 56, 541
- Hughes, A. M., Lieman-Sifry, J., Flaherty, K. M., et al. 2017, *ApJ*, 839, 86
- Jermyn, A. S., Bauer, E. B., Schwab, J., et al. 2023, *ApJS*, 265, 15
- Johnstone, C. P., Jardine, M., Gregory, S. G., Donati, J. F., & Hussain, G. 2014, *MNRAS*, 437, 3202
- Klusmeyer, J., Hughes, A. M., Matrà, L., et al. 2021, *ApJ*, 921, 56
- Koerner, D. W., Sargent, A. I., & Beckwith, S. V. W. 1993, *Icarus*, 106, 2
- Kóspál, Á., Moór, A., Juhász, A., et al. 2013, *The Astrophysical Journal*, 776, 77
- Kral, Q., Marino, S., Wyatt, M. C., Kama, M., & Matrà, L. 2019, *MNRAS*, 489, 3670
- Kral, Q., Matrà, L., Wyatt, M. C., & Kennedy, G. M. 2017, *MNRAS*, 469, 521
- Krivov, A. V., & Wyatt, M. C. 2021, *MNRAS*, 500, 718
- Kunitomo, M., Guillot, T., Takeuchi, T., & Ida, S. 2017, *A&A*, 599, A49
- Lopez, B., Knee, L. B. G., Jager, H., et al. 2014, in *Society of Photo-Optical Instrumentation Engineers (SPIE) Conference Series*, Vol. 9150, *Modeling, Systems Engineering, and Project Management for Astronomy VI*, ed. G. Z. Angeli & P. Dierickx, 91500B
- MacGregor, M. A., Wilner, D. J., Czekala, I., et al. 2017, *ApJ*, 835, 17
- Mannings, V., & Barlow, M. J. 1998, *ApJ*, 497, 330

- Mathieu, R. D., Casey, B., Vaz, L. P., et al. 1994, in American Astronomical Society Meeting Abstracts, Vol. 184, American Astronomical Society Meeting Abstracts #184, 44.08
- Matrà, L., Marino, S., Kennedy, G. M., et al. 2018, ApJ, 859, 72
- McMullin, J. P., Waters, B., Schiebel, D., Young, W., & Golap, K. 2007, in Astronomical Society of the Pacific Conference Series, Vol. 376, Astronomical Data Analysis Software and Systems XVI, ed. R. A. Shaw, F. Hill, & D. J. Bell, 127
- Miley, J. M., Panić, O., Wyatt, M., & Kennedy, G. M. 2018a, A&A, 615, L10
- . 2018b, A&A, 615, L10
- Moór, A., Ábrahám, P., Derekas, A., et al. 2006, ApJ, 644, 525
- Moór, A., Curé, M., Kóspál, Á., et al. 2017, ApJ, 849, 123
- Moór, A., Ábrahám, P., Szabó, G., et al. 2021, ApJ, 910, 27
- Olofsson, J., Milli, J., Bayo, A., Henning, T., & Engler, N. 2020, A&A, 640, A12
- Ono, T., & Shimaoka, H. 1984, Transactions of the Society of Instrument and Control Engineers, 20, 322
- Paxton, B., Bildsten, L., Dotter, A., et al. 2011, ApJS, 192, 3
- Paxton, B., Cantiello, M., Arras, P., et al. 2013, ApJS, 208, 4
- Paxton, B., Marchant, P., Schwab, J., et al. 2015, ApJS, 220, 15
- Paxton, B., Schwab, J., Bauer, E. B., et al. 2018, ApJS, 234, 34

- Paxton, B., Smolec, R., Schwab, J., et al. 2019, *ApJS*, 243, 10
- Pearce, T. D., Launhardt, R., Ostermann, R., et al. 2022, *A&A*, 659, A135
- Pecaut, M. J., & Mamajek, E. E. 2016, *MNRAS*, 461, 794
- Pegues, J., Czekala, I., Andrews, S. M., et al. 2021, *ApJ*, 908, 42
- Perrot, C., Olofsson, J., Kral, Q., et al. 2023, arXiv e-prints, arXiv:2302.07057
- Plavchan, P., Barclay, T., Gagné, J., et al. 2020, *Nature*, 582, 497
- Poppe, T., Blum, J., & Henning, T. 2000, *ApJ*, 533, 472
- Rebollido, I., Eiroa, C., Montesinos, B., et al. 2018, *A&A*, 614, A3
- Ricci, L., Cazzoletti, P., Czekala, I., et al. 2017, *AJ*, 154, 24
- Rollins, R. P., & Rawlings, J. M. C. 2012, *Monthly Notices of the Royal Astronomical Society*, 427, 2328
- Rosenfeld, K. A., Andrews, S. M., Hughes, A. M., Wilner, D. J., & Qi, C. 2013, *ApJ*, 774, 16
- Rosenfeld, K. A., Andrews, S. M., Wilner, D. J., & Stempels, H. C. 2012, *ApJ*, 759, 119
- Sheehan, P. D., Wu, Y.-L., Eisner, J. A., & Tobin, J. J. 2019, *ApJ*, 874, 136
- Simon, M. 2001, in *The Formation of Binary Stars*, ed. H. Zinnecker & R. Mathieu, Vol. 200, 454
- Simon, M., Dutrey, A., & Guilloteau, S. 2000, *ApJ*, 545, 1034
- Simon, M., Schaefer, G. H., Prato, L., et al. 2013, *ApJ*, 773, 28

- Simon, M., & Toraskar, J. 2017, *ApJ*, 841, 95
- Simon, M., Guilloteau, S., Di Folco, E., et al. 2017, *ApJ*, 844, 158
- Simon, M., Guilloteau, S., Beck, T. L., et al. 2019, *ApJ*, 884, 42
- Slawson, R. W., Hill, R. J., & Landstreet, J. D. 1992, *ApJS*, 82, 117
- Smirnov-Pinchukov, G. V., Moór, A., Semenov, D. A., et al. 2022, *MNRAS*, 510, 1148
- Strassmeier, K. G., & Ilyin, I. V. 2009, in *Astrophysics and Space Science Proceedings*, Vol. 9, Science with the VLT in the ELT Era, 255
- Sylvester, R. J., Dunkin, S. K., & Barlow, M. J. 2001, *MNRAS*, 327, 133
- Tazzari, M., Beaujean, F., & Testi, L. 2018, *MNRAS*, 476, 4527
- Vacca, W. D., & Sandell, G. 2011, *ApJ*, 732, 8
- Vidotto, A. A., Gregory, S. G., Jardine, M., et al. 2014, *MNRAS*, 441, 2361
- Virtanen, P., Gommers, R., Oliphant, T. E., et al. 2020, *Nature Methods*, 17, 261
- Visser, R., van Dishoeck, E. F., & Black, J. H. 2009, *A&A*, 503, 323
- Wes McKinney. 2010, in *Proceedings of the 9th Python in Science Conference*, ed. Stéfan van der Walt & Jarrod Millman, 56 – 61
- Wichittanakom, C., Oudmaijer, R. D., Fairlamb, J. R., et al. 2020, *VizieR Online Data Catalog*, J/MNRAS/493/234
- Williams, J. P., & Cieza, L. A. 2011, *Annual Review of Astronomy and Astrophysics*, 49, 67

Wyatt, M. C. 2008, *ARA&A*, 46, 339

Wyatt, M. C., Panić, O., Kennedy, G. M., & Matrà, L. 2015, *Ap&SS*, 357, 103

Zhang, X., Green, G. M., & Rix, H.-W. 2023, arXiv e-prints, arXiv:2303.03420

Zuckerman, B., & Song, I. 2012, *ApJ*, 758, 77